



On a Spectral Method for β -particle Bound Excitation Collisions in Kilonovae

Ryan T. Wollaeger^{1,2} , Chris L. Fryer^{1,3,4,5,6} , Robert M. Chiodi² , Peter T. Brady² , Oleg Korobkin^{1,7} ,
Cale C. Harnish² , Christopher J. Fontes^{1,8} , Jeffrey R. Haack² , Oleksandr Chapurin⁷ , Oleksandr Koshkarov⁷ ,
Gian Luca Delzanno⁷ , and Daniel Livescu²

¹ Center for Theoretical Astrophysics, Los Alamos National Laboratory, Los Alamos, NM 87545, USA

² Computer, Computational, and Statistical Sciences Division, Los Alamos National Laboratory, Los Alamos, NM 87545, USA

³ Center for Nonlinear Studies, Los Alamos National Laboratory, Los Alamos, NM 87545, USA

⁴ The University of Arizona, Tucson, AZ 85721, USA

⁵ Department of Physics and Astronomy, The University of New Mexico, Albuquerque, NM 87131, USA

⁶ The George Washington University, Washington, DC 20052, USA

⁷ T-5 Applied Mathematics and Plasma Physics Group, Los Alamos National Laboratory, Los Alamos, NM 87545, USA

⁸ Computational Physics Division, Los Alamos National Laboratory, Los Alamos, NM 87545, USA

Received 2024 January 19; revised 2024 March 15; accepted 2024 March 24; published 2024 May 6

Abstract

The interaction of β -particles with the weakly ionized plasma background is an important mechanism for powering the kilonova (KN) transient signal from neutron star mergers. For this purpose, we present an implementation of the approximate fast-particle collision kernel, described by Inokuti following the seminal formulation of Bethe, in a spectral solver of the Vlasov–Maxwell–Boltzmann equation. In particular, we expand the fast-particle plane-wave atomic excitation kernel into coefficients of the Hermite basis, and derive the relevant discrete spectral system. In this fast-particle limit, the approach permits the direct use of atomic data, including optical oscillator strengths, normally applied to photon–matter interaction. The resulting spectral matrix is implemented in the MASS-APP spectral solver framework, in a way that avoids full matrix storage per spatial zone. We numerically verify aspects of the matrix construction, and present a proof-of-principle 3D simulation of a 2D axisymmetric KN ejecta snapshot. Our preliminary numerical results indicate that a reasonable choice of Hermite basis parameters for β -particles in the KN is a bulk velocity parameter $\mathbf{u} = 0$, a thermal velocity parameter $\alpha = 0.5c$, and a $9 \times 9 \times 9$ mode velocity basis set (Hermite orders of 0–8 in each dimension). For interior-ejecta sample zones, we estimate that the ratio of thermalization from large-angle ($\gtrsim 2^\circ$) bound excitation scattering to total thermalization is ~ 0.002 – 0.003 .

Unified Astronomy Thesaurus concepts: Neutron stars (1108); Plasma physics (2089)

1. Introduction

Kilonovae (KNe) are radioactively powered electromagnetic (EM) transients signaling the aftermath of double-neutron star or neutron star–black hole binary mergers (an incomplete sequence of kilonova (KN) model developments up to 2017 might be given by Lattimer & Schramm 1974, 1976; Li & Paczyński 1998; Freiburghaus et al. Freiburghaus 1999; Roberts et al. 2011; Kasen et al. 2013; Tanaka & Hotokezaka 2013; Fontes et al. 2015a; Barnes et al. 2016; Metzger 2017). As the two compact objects inspiral due to the emission of gravitational waves, the neutron star(s) will be tidally disrupted, causing neutron-rich mass to eject and become gravitationally unbound. The merger results in a compact remnant (neutron star or black hole) surrounded by an accretion disk, from which various mechanisms produce further (*post-merger*) ejecta (see, for example, Perego et al. 2014; Martin et al. 2015; Desai et al. 2022). The detailed EM spectra and broadband magnitudes from the observation of KN AT2017gfo (see, for example, Arcavi et al. 2017; Cowperthwaite et al. 2017; Drout et al. 2017; Kasliwal et al. 2017; Smartt et al. 2017; Tanvir et al. 2017; Troja et al. 2017; Villar et al. 2017), in concert with the gravitational-wave observation GW170817 (Abbott et al. 2017a, 2017b), provided an

unprecedented window into the pre- and post-merger phases of the transient, and by examining the nuclear decay pattern in the ejecta seemed to confirm neutron star mergers are a source of r -process elements (Rosswog et al. 2018).

While the basic picture of KNe has remained unchanged for several decades since the semi-analytic work of Li & Paczyński (1998; for a review of KN physics, see also Metzger 2019), simulating KNe at high fidelity is an ever-developing field. Recent studies have explored detailed radiative transfer, atomic physics, non-local thermodynamic equilibrium (non-LTE), and multidimensional spatial ejecta; see, for instance, Fontes et al. (2020), Tanaka et al. (2020), Fontes et al. (2023) on detailed LTE opacity, Hotokezaka et al. (2021), Pognan et al. (2022a), Pognan et al. (2022b, 2023) on detailed non-LTE opacity, and Heinzl et al. (2021), Korobkin et al. (2021), Bulla (2023), and Fryer et al. (2024) on spatial distribution and multidimensional spatial effects (and see references therein). Each of these aspects brings a level of uncertainty into the simulations that otherwise might be encapsulated in free parameters (for example, gray opacity). A large source of uncertainty in state-of-the-art calculations, particularly at late times as the KN ejecta becomes nebular, is in modeling the interaction of decay products (α , β , and γ particles) with the ions forming the ejecta. In full generality, it is a complicated problem of multiple particle fields undergoing transfer and interaction with atomic orbital structure and free electrons. Moreover, the atomic structure of the elements formed in the r -process can involve tens of millions of resonances between thousands to millions of



Original content from this work may be used under the terms of the [Creative Commons Attribution 4.0 licence](https://creativecommons.org/licenses/by/4.0/). Any further distribution of this work must maintain attribution to the author(s) and the title of the work, journal citation and DOI.

energy levels (see, for example, the atomic data presented by Fontes et al. 2020; Tanaka et al. 2020).

The process of β -particle thermalization (the loss of particle kinetic energy to Coulomb interactions, atomic excitations, ionizations, etc.) is inefficient compared to thermalization of the more massive α -particles or fission fragments (Barnes et al. 2016, 2021; Zhu et al. 2021), and hence is nonlocal (β -particles travel significant length scales relative to the ejecta to deposit energy). Barnes et al. (2016, 2021) and Zhu et al. (2021) have demonstrated that this inefficiency significantly impacts the observable EM KN signal (on the order of a factor of 2 in luminosity, for instance). The state-of-the-art detailed thermalization model for β -particles presented by Barnes et al. (2021) uses the Bethe stopping potential prescription (Bethe 1930), which accounts for energy loss over a particle path, due to multiple small-angle scatters and encapsulates atomic properties with an average ionization. A question remains as to the impact of large-angle scatters that induce excitation effects in the ion background, which in principle requires the so-called *generalized* oscillator strengths that were introduced by Bethe (1930) and elaborated on by Inokuti (1971).

Consequently, having a framework for implementing atomic data directly into a thermalization calculation, along with a formulation for particle transfer that can be extended to different differential cross sections, is useful for making inroads to improved fidelity. We attempt one such preliminary inroad using a deterministic spectral plasma solver implemented in the CPU/GPU-parallel Multiphysics Adaptive Scalable Simulator for Applications in Plasma Physics (MASS-APP) code base (R. Chiodi & P. T. Brady et al. 2024, in preparation). *Spectral* in this context implies the particle phase space distribution function is expanded over a complete basis function set in velocity space. To undertake proof-of-concept simulations, we implement the nonrelativistic inelastic scattering kernel for excitation, as described by Inokuti (1971). The inelastic form of the two-body, or binary, integral collision kernel is given by Garibotti & Spiga (1994), and has been used before in the context of spectral Boltzmann methods (see, for instance, the spectral Lagrangian Boltzmann equation solver by Munafò et al. 2014). Here, we specifically employ an asymmetrically weighted Hermite function basis (Armstrong et al. 1970), which has the beneficial property of bridging macro (fluid)-micro (kinetic) scales (see, for example, Camporeale et al. 2006; Delzanno 2015; Vencels et al. 2015; Koshkarov et al. 2021). The derivational sequence we present here is similar to the Hermite expansion of the multispecies collision kernel presented by Wang & Cai (2019) and Li et al. (2022, 2023), but we do not expand both distributions into the binary kernel, instead expanding one and also expanding the cross section itself in the Hermite basis. We also make approximations to the kernel that make the integral over the ion species separable from the integral over β -particle velocity (which generally will not hold outside the fast-particle approximation). This permits us to employ an efficient closed form for integrals of products involving three Hermite polynomials and two Gaussian weights, which to our knowledge, was not used by Wang & Cai (2019) or Li et al. (2022, 2023) since their kernel expansion does not isolate these terms (to be sure, the approaches of these authors are more general, in being able to solve for multiple distribution species).

Neglecting internal conversion, β -particle emission has a smooth continuum (Fermi 1934; Schenter & Vogel 1983;

Alekseev et al. 2020) for a spectrum, lending itself well to smooth basis functions. Hence, we see this spectral Hermite basis technique as a possible deterministic supplement to particle-in-cell or Monte Carlo methods that may be better suited to treating sharp electron emission lines resulting from internal conversion. Moreover, deterministic schemes, of course, do not have stochastic noise, so they may be well suited to capturing large-angle scattering effects, specifically.

This paper is organized as follows. In Section 2, we write the governing equation solved with MASS-APP and describe the derivation of the excitation collision kernel used for β -particles. In Section 3, we present numerical verification of particular aspects of the method, comparing closed-form derivations to direct numerical integration of terms that build the collision matrix needed for simulation. In Section 4, we describe a trial β -particle simulation of excitation interactions for a 2D axisymmetric morphology embedded in 3D Cartesian geometry. Finally, in Section 5, we summarize our findings and discuss future work that would further improve fidelity.

2. Spectral Method and Implementation

In this section, we write down the full spectrally discretized set of equations. Subsequently, we focus attention on incorporating the nonrelativistic differential excitation cross section given by Inokuti (1971) into the spectral basis framework and discuss the approximations made to simplify the collision kernel. After deriving the spectral Hermite form of the fast-particle kernel, we provide an outline summarizing the calculations of this section, including how the steps may be extensible to other differential cross sections. Supplementary detail is provided in Appendix A for the evaluation of the two-body collision kernel and in Appendix B for the evaluation of the closed-form of integrals involving three Hermite polynomials and two Gaussian weight functions, referred to henceforth as *compact triple-Hermite products*, which are used to evaluate each term in the spectrally discrete collision matrix derived in this section.

The Vlasov–Maxwell–Boltzmann system of equations we consider is

$$\frac{\partial f_s}{\partial t} + \mathbf{v} \cdot \nabla f_s + \frac{q_s}{m_s} (\mathbf{E} + \mathbf{v} \times \mathbf{B}) \cdot \nabla_v f_s = \mathcal{C}[f_a, f_s], \quad (1a)$$

$$\frac{\partial \mathbf{E}}{\partial t} = c \nabla \times \mathbf{B} - 4\pi \mathbf{J}, \quad (1b)$$

$$\frac{\partial \mathbf{B}}{\partial t} = -c \nabla \times \mathbf{E}, \quad (1c)$$

$$\mathbf{J} = q_s \int \mathbf{v} f_s d^3\mathbf{v} + q_a \int \mathbf{v} f_a d^3\mathbf{v}, \quad (1d)$$

where t is time, \mathbf{v} is velocity, the ∇ operator is the gradient with respect to the spatial coordinate (\mathbf{x}), ∇_v is the gradient operator with respect to velocity, subscript s indicates the species (β -particles here), subscript a indicates the atom/ion background, q_s is the charge, m_s is mass, \mathbf{E} and \mathbf{B} are the electric and magnetic fields, f_s and f_a are the β -particle and background distributions (number density per spatial volume per velocity volume), \mathbf{J} is the current density, and $\mathcal{C}[\cdot, \cdot]$ is the collision operator. For the purpose of this work, we set the interacting distribution of ejecta atom/ions as given within a discrete time step, thus linearizing the collision term. This approach is consistent with the practice of computing decay thermalization

and radiative transfer in separate steps from the update of the ejecta plasma state but may incur errors where moderate bulk thermodynamic changes lead to a significant discrepancy in the electron occupation number for particular atomic states.

The Hermite basis is orthogonal with respect to a Gaussian weight, and hence is amenable to determining expansion coefficients via inner products. Following Delzanno (2015), we expand the distribution as

$$f_s(\mathbf{x}, \mathbf{v}, t) = \sum_{n,m,p} C_{n,m,p}(\mathbf{x}, t) \Psi_{n,m,p}(\boldsymbol{\xi}), \quad (2)$$

where the subscripts n , m , and p are the order of the basis function in each velocity dimension, $C_{n,m,p}$ is the expansion coefficient (for which we solve), and the basis function $\Psi_{n,m,p}(\boldsymbol{\xi})$ is given by Equation (B3). The $\boldsymbol{\xi}$ argument of the basis functions is the nondimensional velocity (subscript xyz indicates the components),

$$\begin{aligned} \boldsymbol{\xi} &= (\xi_x, \xi_y, \xi_z) = \left(\frac{v_x - u_x}{\alpha_x}, \frac{v_y - u_y}{\alpha_y}, \frac{v_z - u_z}{\alpha_z} \right) \\ &= (\mathbf{v} - \mathbf{u}) \oslash \boldsymbol{\alpha}, \end{aligned} \quad (3)$$

where \mathbf{u} and $\boldsymbol{\alpha}$ are user-provided, constant velocity parameters corresponding to bulk and thermal velocity in the Gaussian factor of the basis. The last equality represents $\boldsymbol{\xi}$ with Hadamard (element-wise) division.

The system of equation resulting from expanding Equation (1) with Equation (2) and taking inner Hermite products is (see, for example, Delzanno 2015)

$$\frac{\partial C_{n,m,p}}{\partial t} + \dots = \sum_{n',m',p'} S_{n,m,p}^{n',m',p'} C_{n',m',p'}, \quad (4a)$$

$$\frac{\partial \mathbf{B}}{\partial t} = -c \nabla \times \mathbf{E}, \quad (4b)$$

$$\frac{\partial \mathbf{E}}{\partial t} = c \nabla \times \mathbf{B} - 4\pi q_s \alpha_x \alpha_y \alpha_z \left(C_{0,0,0} \begin{bmatrix} u_x \\ u_y \\ u_z \end{bmatrix} + \frac{1}{\sqrt{2}} \begin{bmatrix} \dots \\ \dots \\ \dots \end{bmatrix} \right) \quad (4c)$$

where $S_{n,m,p}^{n',m',p'}$ is a collision matrix dependent on the background ion properties of the KN ejecta, and in Equation (4c) we have made the approximation that the ion background does not contribute significant current density. For brevity, on the left side of Equation (4a), we have omitted a spatial divergence operator, including the flux and Lorentz force from \mathbf{E} and \mathbf{B} , but include them in a version of the equation in Appendix C.

2.1. Fast-particle, Nonrelativistic, Differential Cross Section

We derive the nonrelativistic form of the scattering matrix $S_{n,m,p}^{n',m',p'}$ using the differential cross section in the Bethe–Born (high-energy) limit, presented by Inokuti (1971) for excitation from atomic state j' to atomic state j ,

$$\frac{d\sigma_{jj'}}{d\Omega} = 4 \left(\frac{Me^2}{\hbar^2} \right)^2 \left(\frac{k'}{k} \right) K^{-4} \left(\frac{R}{E_{jj'}} \right) (Ka_0)^2 f_{jj'}(K), \quad (5)$$

where

$$M = \frac{m_e M_a}{m_e + M_a} \quad (6)$$

is the reduced mass (m_e and M_a are electron and atomic mass), e is the electron charge, \hbar is the reduced Planck constant, k (k') is the incoming (outgoing) wavenumber (equivalently momentum $=\hbar k$) of the free electron, K is the magnitude of the difference between the incoming and outgoing wavenumbers, $R = m_e e^4 / 2\hbar^2 = 13.606$ eV is the Rydberg energy, $E_{jj'}$ is the energy difference between levels j and j' , $a_0 = \hbar^2 / (m_e e^2) = 0.52918 \times 10^{-8}$ cm is the Bohr radius, and $f_{jj'}(K)$ is the generalized oscillator strength. The magnitudes of the wavenumber obey the law of cosines,

$$K^2 = k^2 + (k')^2 - 2k'k \cos(\theta), \quad (7)$$

where θ is the polar angle of deflection in the center-of-mass frame. If the magnitude of pre- and post-deflection wavenumbers is taken to be independent of the polar deflection angle, then

$$\frac{d(K^2)}{d\theta} = 2k'k \sin(\theta), \quad (8)$$

which is given by Inokuti (1971) to replace the solid angle differential $d\Omega$ with $d(K^2)$. Assuming $k' = k$, then $K^2 = 2k^2(1 - \cos(\theta)) = 4k^2 \sin^2(\theta/2)$, and Equation (5) becomes

$$\frac{d\sigma_{jj'}}{d\Omega} = \left(\frac{Me^2}{\hbar^2} \right)^2 \frac{\csc^4(\theta/2)}{4k^4} \left[\left(\frac{R}{E_{jj'}} \right) (Ka_0)^2 f_{jj'}(K) \right], \quad (9)$$

Supposing an elastic collision, conservation of kinetic energy and momentum imply

$$k' = k \left(\frac{\cos(\theta) + \sqrt{(M_a/m_e)^2 - \sin^2(\theta)}}{1 + M_a/m_e} \right), \quad (10)$$

where the higher root is taken, so that the solution would be correct if $M_a = m_e$. Consequently,

$$\lim_{M_a/m_e \rightarrow \infty} k' = k, \quad (11)$$

so the condition of $k' = k$, giving Equation (9) is equivalent to $m_e \ll M_a$ for elastic collisions. Also, in this limit, the reduced mass converges to the electron mass m_e , and noting $\hbar k = m_e v_0$, where v_0 is the initial electron velocity, Equation (9) becomes

$$\frac{d\sigma_{jj'}}{d\Omega} = \left(\frac{e^2}{2m_e v_0^2} \right)^2 \csc^4(\theta/2) \left[\left(\frac{R}{E_{jj'}} \right) (Ka_0)^2 f_{jj'}(K) \right], \quad (12)$$

where the coefficient outside the brackets on the right side is now the standard nonrelativistic definition of classical Rutherford scattering (a more general form is noted by Inokuti 1971 as the coefficient, not making the assumption of $m_e \ll M_a$). According to Inokuti (1971), the term in the square brackets is the conditional probability that the atom will excite from state j' to state j , given a magnitude of momentum exchange from the electron of K .

It is notable that $k = k'$ does not imply that K is small; the angle θ has to vanish for K to vanish. Using Equation (7) and

conservation of kinetic energy, balanced with excitation, the formula for $(Ka_0)^2$ in terms of initial electron kinetic energy $E_k = mv_0^2/2$ and θ is (Inokuti 1971)

$$(Ka_0)^2 = 2 \frac{E_k}{R} \left(\frac{M}{m_e} \right)^2 \times \left[1 - \frac{1}{2} \left(\frac{m_e E_{jj'}}{ME_k} \right) - \left(\sqrt{1 - \left(\frac{m_e E_{jj'}}{ME_k} \right)} \right) \cos(\theta) \right]. \quad (13)$$

$(Ka_0)^2$ has the following limits, corresponding to $\theta = 0$ or π in Equation (13) (Inokuti 1971):

$$(Ka_0)_{\min}^2 \approx \frac{1}{4} \left(\frac{E_{jj'}^2}{RE_k} \right) \left[1 + \frac{1}{2} \left(\frac{m_e E_{jj'}}{MR} \right) \right], \quad (14a)$$

$$(Ka_0)_{\max}^2 \approx 4 \frac{E_k}{R} \left(\frac{M}{m_e} \right)^2 \left[1 - \frac{1}{2} \left(\frac{m_e E_{jj'}}{ME_k} \right) \right], \quad (14b)$$

where the square root coefficient of $\cos(\theta)$ has been Taylor expanded in $m_e E_{jj'}/(ME_k)$ (Inokuti 1971). The assumption is that $E_k \gg E_{jj'}$ and $E_k \gg R$ implies the maximum value of $(Ka_0)_{\max}^2 \gg 1$. However, the Rutherford coefficient of Equation (12) grows rapidly as θ vanishes. Moreover, the generalized oscillator strength decreases rapidly for large Ka_0 (see Inokuti 1971, Section 3.2). Thus, low Ka_0 and small-angle deflections, i.e., forwarding scattering, are most probable from the Bethe kernel. If the generalized oscillator strength is expanded in a Taylor series as a function of Ka_0 (Inokuti 1971), and assuming $(Ka_0)^2 \sim (Ka_0)_{\min}^2$, due to the dominance of forward scattering, it becomes reasonable to replace the generalized oscillator strength with the optical oscillator strength, $f_{jj'} \approx f_{jj'}(K=0)$, which is the essence of the Bethe high-energy approximation.

If we take $f_{jj'} = f_{jj'}(K=0)$, we may readily use the oscillator strength data used for photon opacities in Equation (12). Doing so, and also incorporating Equation (13) into Equation (12), we have a nonrelativistic excitation cross section from state j' to state j ,

$$\frac{d\sigma_{jj'}}{d\Omega} = 2 \left(\frac{e^2}{4E_k} \right)^2 \csc^4(\theta/2) \left(\frac{E_k}{E_{jj'}} \right) f_{jj'} \times \left[1 - \frac{1}{2} \left(\frac{E_{jj'}}{E_k} \right) - \left(\sqrt{1 - \left(\frac{E_{jj'}}{E_k} \right)} \right) \cos(\theta) \right], \quad (15)$$

where $m_e = M$ has been incorporated into Equation (13). The only quantity with units on the right side is $(e^2/4E_k)^2$, which should have units of length squared. In electrostatic cgs units (used by Inokuti 1971), so

$$\left(\frac{e^2}{4E_k} \right)^2 \approx \left(\frac{197}{548} \frac{1}{E_{k,\text{MeV}}} \right)^2 \text{fm}^2, \quad (16)$$

where $E_{k,\text{MeV}}$ is the initial kinetic energy in MeV and fm = femtometers.

2.2. Spectral Matrix from a Binary Collision Kernel

We now incorporate Equation (15) into the two-body inelastic collision kernel (the elastic version is given by

Mihalas & Mihalas 1984, Chapter 1, for example). For our purpose, we decompose the atomic distribution into sub-distributions corresponding to each excited state j' , and expand the collision kernel as follows:

$$\mathcal{C}[f_a, f_s] = \sum_{(jj') \in \mathcal{T}} \mathcal{C}_{jj'}[f_{a,j'}, f_{a,j}, f_s], \quad (17)$$

where \mathcal{T} is the set of possible state transition pairs (j, j') ,

$$\mathcal{C}_{jj'}[f_{a,j'}, f_{a,j}, f_s] = \iint |\mathbf{v}_a - \mathbf{v}_s| \frac{d\sigma_{jj'}}{d\Omega} \times \left(\frac{g_j'}{g_j} f_s(\mathbf{v}_s') f_{a,j}(\mathbf{v}_a') - f_s(\mathbf{v}_s) f_{a,j'}(\mathbf{v}_a) \right) d\Omega d^3\mathbf{v}_a, \quad (18)$$

and we have subscripted velocities to indicate ion (“a”) or β -particle (“s”). We note this expression follows Munafò et al. (2014), where the energy level degeneracy is included as a coefficient of the product of distributions over post-scatter velocities. The distribution prime superscript indicates evaluation at the post-collision momentum.

Post-scatter velocities \mathbf{v}_a' and \mathbf{v}_s' can be evaluated from the conservation of momentum and energy in the nonrelativistic limit, giving

$$\mathbf{v}_s' = \frac{1}{m_e + M_a} \left(m_e \mathbf{v}_s + M_a \mathbf{v}_a + M_a \left(\sqrt{v_{sa}^2 - \frac{2E_{jj'}}{M}} \right) \hat{\Omega}' \right), \quad (19a)$$

$$\mathbf{v}_a' = \frac{1}{m_e + M_a} \left(m_e \mathbf{v}_s + M_a \mathbf{v}_a - m_e \left(\sqrt{v_{sa}^2 - \frac{2E_{jj'}}{M}} \right) \hat{\Omega}' \right), \quad (19b)$$

where $v_{sa} = |\mathbf{v}_{sa}| = |\mathbf{v}_a - \mathbf{v}_s|$. Equation (19) shows the post-scatter velocities as a function of pre-scatter velocity and energy weight, which must be incorporated into Equation (18) to evaluate the post-scatter portion of the integral (Garibotti & Spiga 1994).

Considering only excitation collisions in Equation (1), and expanding the β -distribution f_s with Equation (3),

$$\begin{aligned} & \sum_{n,m,p} \frac{\partial C_{n,m,p}}{\partial t} \Psi_{n,m,p}(\boldsymbol{\xi}) \\ &= \sum_{n,m,p} C_{n,m,p} \iint v_{sa} \frac{d\sigma_{jj'}}{d\Omega} \frac{g_j'}{g_j} \Psi_{n,m,p}(\boldsymbol{\xi}') f_{a,j}(\mathbf{v}_a') d\Omega d^3\mathbf{v}_a \\ & - \sum_{n,m,p} C_{n,m,p} \iint v_{sa} \frac{d\sigma_{jj'}}{d\Omega} \Psi_{n,m,p}(\boldsymbol{\xi}) f_{a,j'}(\mathbf{v}_a) d\Omega d^3\mathbf{v}_a, \end{aligned} \quad (20)$$

where ξ' is the nondimensional form of the post-scatter velocity \mathbf{v}_s' . Taking the inner basis product, Equation (20) becomes

$$\begin{aligned} \frac{\partial C_{n',m',p'}}{\partial t} &= \sum_{n,m,p} C_{n,m,p} \int \Psi^{n',m',p'}(\xi) \iint v_{sa} \frac{d\sigma_{jj'}}{d\Omega} \\ &\times \frac{g_j'}{g_j} \Psi_{n,m,p}(\xi') f_{a,j}(\mathbf{v}'_a) d\Omega d^3\mathbf{v}_a d^3\xi \\ &- \sum_{n,m,p} C_{n,m,p} \int \Psi^{n',m',p'}(\xi) \iint v_{sa} \frac{d\sigma_{jj'}}{d\Omega} \\ &\times \Psi_{n,m,p}(\xi) f_{a,j'}(\mathbf{v}_a) d\Omega d^3\mathbf{v}_a d^3\xi. \end{aligned} \quad (21)$$

The right side of Equation (21) is now in the form of a matrix product with the spectral solution vector $C_{n,m,p}$, as in the right side of Equation (4). Following Munafò et al. (2014), the integral in the first summation on the right side of Equation (21) permits us to use the principle of microreversibility,

$$v_{sa} \frac{d\sigma_{jj'}}{d\Omega} d\Omega d^3\mathbf{v}_a d^3\xi = \frac{g_j}{g_j'} v'_{sa} \frac{d\sigma_{j'j}}{d\Omega'} d\Omega' d^3\mathbf{v}'_a d^3\xi', \quad (22)$$

where we have taken $d\Omega'$ to be the differential solid angle about the pre-scatter direction $\hat{\Omega}$, to simplify Equation (21) to

$$\begin{aligned} \frac{\partial C_{n',m',p'}}{\partial t} &= \sum_{n,m,p} C_{n,m,p} \left[\iint v'_{sa} \left(\int \Psi^{n',m',p'}(\xi(\xi', \mathbf{v}'_a, \bar{\Omega})) \right. \right. \\ &\times \left. \left. \frac{d\sigma_{j'j}}{d\Omega'} \right) \Psi_{n,m,p}(\xi') f_{a,j}(\mathbf{v}'_a) d^3\mathbf{v}'_a d^3\xi' \right. \\ &\left. - \int \Psi^{n',m',p'}(\xi) \int v_{sa} \left(\int \frac{d\sigma_{jj'}}{d\Omega} \right) \Psi_{n,m,p}(\xi) f_{a,j'}(\mathbf{v}_a) d^3\mathbf{v}_a d^3\xi \right] \end{aligned} \quad (23)$$

However, the upper-index basis is still a function of pre-scatter velocity ξ , which is now a function of the post-scatter velocities and collision angle (time-inverting Equation (19)).

In order to further simplify Equation (23), we make some approximations that should be reasonable, at least for the fast-particle approximation and the conditions of the proper inertial frame of the KN ejecta. The first approximation is to evaluate $\Psi^{n',m',p'}(\xi(\xi', \mathbf{v}'_a, \bar{\Omega}))$ at assumed average values of 0 for the pre-scatter angle $\bar{\Omega}$ and the post-scatter ion velocity \mathbf{v}_a , thus permitting factoring out $\Psi^{n',m',p'}$ from the first integral, giving

$$\begin{aligned} \frac{\partial C_{n',m',p'}}{\partial t} &= \sum_{n,m,p} C_{n,m,p} \left[\int \int v_{sa} \Psi^{n',m',p'} \right. \\ &\times \left(\frac{1}{m_e + M_a} (m_e \xi' - M_a \mathbf{u} \oslash \alpha) \right) \sigma_{j'j} \Psi_{n,m,p}(\xi') f_{a,j}(\mathbf{v}'_a) d^3\mathbf{v}'_a d^3\xi' \\ &\left. - \int \Psi^{n',m',p'}(\xi) \int v_{sa} \sigma_{jj'} \Psi_{n,m,p}(\xi) f_{a,j'}(\mathbf{v}_a) d^3\mathbf{v}_a d^3\xi \right]. \end{aligned} \quad (24)$$

where use has been made of Equation (19) with the substitution of the 0-averages to obtain the new argument of $\Psi^{n',m',p'}$ in the first integral, and $\mathbf{u} \oslash \alpha$ again denotes the element-wise division of \mathbf{u} by α (Hadamard division). The isolated differential cross sections in the first and second integral have been integrated over pre- and post-scatter solid angles, respectively, giving $\sigma_{j',j}$, and $\sigma_{jj'}$.

The next approximation we make is to truncate a Hermite basis expansion of the angularly integrated cross section,

$$v_{sa} \sigma_{jj'} = f_{jj'} \sum_{n'',m'',p''} D_{n'',m'',p''}(E_{jj'}) \Psi_{n'',m'',p''}(\xi), \quad (25)$$

where we have made use of dependence of E_k on ξ through Equations (3) and (31). This approximation also implicitly assumes $\mathbf{v}_{sa} \approx \mathbf{v}_s$ since the argument of the basis function is ξ , and hence is independent of the ion/atom velocity \mathbf{v}_a . Linearly factoring $f_{jj'}$ in Equation (25) would not be possible if we use generalized oscillator strengths since $f_{jj'}$ would then depend on the particle momentum transfer, as in Equation (12). As we will see numerically in Section 3, in the limit of $E_{jj'} \ll E_k$ for all level pairs (j, j') , given Equation (15) is inversely proportional to $E_{jj'}$ to leading order, $\log(D_{n'',m'',p''}(E_{jj'}))$ is very close to being linear in $\log(E_{jj'})$. This permits us to store $D_{n'',m'',p''}(E_{jj'})$ as a set of two-parameter values that fit linear functions in this log space. Furthermore, the symmetry in the radial velocity of the original kernel implies that $D_{n'',m'',p''}$ is invariant under permutations of (n'', m'', p'') , which permits further savings in data storage.

Incorporating Equation (25) into the first and second terms of Equation (24),

$$\begin{aligned} \frac{\partial C_{n',m',p'}}{\partial t} &= \sum_{n,m,p} C_{n,m,p} \left[\sum_{n'',m'',p''} f_{jj'} D_{n'',m'',p''}(E_{jj'}) \right]^* \\ &\left\{ \int f_{a,j}(\mathbf{v}'_a) d^3\mathbf{v}'_a \int \Psi^{n',m',p'} \left(\frac{1}{m_e + M_a} (m_e \xi' - M_a \mathbf{u} \oslash \alpha) \right) \right. \\ &\times \Psi_{n'',m'',p''}(\xi') \Psi_{n,m,p}(\xi') d^3\xi' \\ &\left. - \int f_{a,j'}(\mathbf{v}_a) d^3\mathbf{v}_a \int \Psi^{n',m',p'}(\xi) \Psi_{n'',m'',p''}(\xi) \Psi_{n,m,p}(\xi) d^3\xi \right\}, \end{aligned} \quad (26)$$

where, given the preceding approximation, the integrals over β -velocity and atom/ion velocity are separable, and hence factored here. We have also used $\sigma_{j'j}(E_{jj'}) = \sigma_{jj'}(E_{jj'})$, under the assumption that permuting the initial and final energy levels does not change the cross-section structure (statistical weights from partition functions factoring in the ion distributions, $f_{a,j}$, break the equality for rates, however).

Given $m_e \ll M_a$, the next approximation we might make is $\Psi^{n',m',p'}((m_e \xi' - M_a \mathbf{u} \oslash \alpha))$, which gives

$$\begin{aligned} \frac{\partial C_{n',m',p'}}{\partial t} &\approx \frac{\partial C_{n',m',p'}}{\partial t} \left(\frac{m_e \xi' - M_a \mathbf{u} \oslash \alpha}{m_e + M_a} \right) \\ &\approx \frac{\partial C_{n',m',p'}}{\partial t} \left(\frac{m_e \xi' - M_a \mathbf{u} \oslash \alpha}{m_e + M_a} \right) \left[\sum_{n'',m'',p''} f_{jj'} D_{n'',m'',p''}(E_{jj'}) \right]^* \\ &\left\{ \Psi^{n',m',p'}(-\mathbf{u} \oslash \alpha) \int f_{a,j}(\mathbf{v}'_a) d^3\mathbf{v}'_a \right. \\ &\times \int \Psi^{0,0,0}(\xi') \Psi_{n'',m'',p''}(\xi') \Psi_{n,m,p}(\xi') d^3\xi' \\ &\left. - \int f_{a,j'}(\mathbf{v}_a) d^3\mathbf{v}_a \int \Psi^{n',m',p'}(\xi) \Psi_{n'',m'',p''}(\xi) \Psi_{n,m,p}(\xi) d^3\xi \right\}, \end{aligned} \quad (27)$$

where we have inserted $\Psi^{0,0,0}(\xi') = 1$ in the integral, in order to show it is now a special case of the second pre-scatter integral. For more generality, we could have expanded $\Psi^{n',m',p'}((m_e \xi' - M_a \mathbf{u} \oslash \alpha)/(m_e + M_a))$ in terms of the upper-index form of the basis, but this does not add significant

formulaic complication (but it does complicate numerical computation).

The triple-basis integrals in Equation (27) are separable by dimension in Cartesian velocity space, resulting in three integrals, where each has an integrand that is a product of three Hermite basis functions: one upper index and two lower indexes. For the two upper indexes and one lower-index Hermite basis, the solution of the integral has been developed via the use of a three-dimensional generator function by Andrews et al. (1999). To evaluate the one upper-index and the two lower-index integrals, we may revisit the generator function approach given by Andrews et al. (1999) to find a closed-form finite sum that embeds the two upper-index, one lower-index version of the function. We provide this derivation in Appendix B, and using the result, Equation (B21), Equation (27) becomes

$$\begin{aligned} \frac{\partial C_{n',m',p'}}{\partial t} = & \sum_{n,m,p} C_{n,m,p} \left[\sum_{n'',m'',p''} f_{jj'} D_{n'',m'',p''}(E_{jj'}) * \right. \\ & \left. \left\{ \Psi^{n',m',p'}(-\mathbf{u} \otimes \boldsymbol{\alpha}) \left(\int f_{a,j}(\mathbf{v}_a) d^3v_a \right) T_c(n, 0, n'') T_c(m, 0, m'') T_c(p, 0, p'') \right. \right. \\ & \left. \left. - \left(\int f_{a,j'}(\mathbf{v}_a) d^3v_a \right) T_c(n, n', n'') T_c(m, m', m'') T_c(p, p, p'') \right\} \right]. \end{aligned} \quad (28)$$

If we are given the ion distribution $f_{a,j}(\mathbf{v}_a)$ for all j and fitting coefficients for $D_{n,m,p}$, we may evaluate the matrix by summing over all pairs (j, j') to get the spectral formulation of Equation (17). Moreover, the ion velocity integrals merely result in the population density for states j and j' , $N_{a,j}$ and $N_{a,j'}$. The result is

$$\begin{aligned} \frac{\partial C_{n',m',p'}}{\partial t} = & \sum_{n,m,p} C_{n,m,p} \\ & \times \left[\sum_{n'',m'',p''} \left\{ \Psi^{n',m',p'}(-\mathbf{u} \otimes \boldsymbol{\alpha}) D_{n'',m'',p''}^{(U)}(\mathbf{x}, t) T_c(n, 0, n'') T_c(m, 0, m'') T_c(p, 0, p'') \right. \right. \\ & \left. \left. - D_{n'',m'',p''}^{(L)}(\mathbf{x}, t) T_c(n, n', n'') T_c(m, m', m'') T_c(p, p, p'') \right\} \right] \\ = & \sum_{n,m,p} C_{n,m,p} S_{n,m,p}^{n',m',p'}, \end{aligned} \quad (29)$$

where

$$D_{n,m,p}^{(L)}(\mathbf{x}, t) = \sum_{(j',j) \in \mathcal{T}} N_{a,j'}(\mathbf{x}, t) f_{jj'} D_{n,m,p}(E_{jj'}), \quad (30a)$$

$$D_{n,m,p}^{(U)}(\mathbf{x}, t) = \sum_{(j',j) \in \mathcal{T}} N_{a,j}(\mathbf{x}, t) f_{jj'} D_{n,m,p}(E_{jj'}). \quad (30b)$$

Similar to $D_{n,m,p}$, the function $T_c(n, n', n'')$ is symmetric under permutation of (n, n', n'') . Furthermore, $D_{n,m,p}$ and $T_c(n, n', n'')$ are spatially invariant functions; the ion distribution ultimately encodes spatial variation in the spectral scattering matrix. The spatial invariance and symmetry under index permutation make $D_{n,m,p}$ and $T_c(n, n', n'')$, as well as the linear fitting representation of $D_{n,m,p}$, very memory efficient in computational storage, compared to the spectral solution $C_{n,m,p}$. For instance, considering the basis symmetry, for $(n, m, p) \in \{0, 1, 2, 3, 4\}^3$, the number of $C_{n,m,p}$ values to store is 125 per spatial zone, while $T_c(n, m, p)$ results in at most 35 distinct floating point values, and $D_{n,m,p}$ results in 35 distinct pairs of floating point values (assuming two-parameter linear fits over atomic transition energy $E_{jj'}$, as discussed). The $T_c(n, m, p)$ function is also made asymptotically $\sim 50\%$ sparse

for large (n, m, p) , by the (n, m, p) parity selection rules discussed in Appendix B.

Specifically for Section 4, our final main approximation is to assume Maxwellian velocity dependence of the ion distribution $f_{a,j}(\mathbf{v}_a)$ and Boltzmann statistics for excitation energy. This is an LTE assumption about the relative population of the excitation states within an ionization stage. While we also restrict our calculations to a single ion stage, we note that Saha statistics (hence the Saha–Boltzmann formulation, for instance, as presented by Mihalas & Mihalas 1984) can be used without complicating the above matrix formulae. For more detail on the integrals using the Maxwellian ion distribution, as well as evaluation of the solid angle integral of the differential cross section, see Appendix A.

2.3. Outline of a General Derivation

To end this section, we note that the calculation procedure described above may translate to a more general derivation sequence applicable to different types of collision kernels. These general steps are outlined here.

1. Identify the optimal coordinate system of velocity space to spectrally expand functional forms of the solution distribution and the differential cross section.
2. Choose one or more spectral bases in the velocity coordinate system based on physics (for example, Gaussian weighting function for inner products, for natural-scale bridging, or relativity-compatible functions such as the Maxwell–Jüttner distribution) and physical regime, and expand both the distribution function and cross section in terms of the basis functions.
3. Determine if parametric fits (for example, in this work over atomic transition energy) are applicable to the fundamental cross-section coefficients ($D_{n,m,p}$).
 - (a) Store the spatially invariant form of the parameterized coefficients if possible (for instance, excluding integration of the coefficient over the atom/ion distribution).
 - (b) Determine any index symmetries to further compress the $D_{n,m,p}$ array.
4. Incorporate the expansions into the collision kernel relating the distribution to the differential cross section.
5. Use the principle of microreversibility to (possibly) simplify the evaluation of the post-scatter term.
6. Determine if approximations, or an expansion, is possible to separate kernel integrals by species (for example, the separation of the integral over ion velocity above).
7. Integrate and use basis orthogonality to arrive at a spectral matrix equation.
8. If possible, use closed-form expressions for basis function triple products (Andrews et al. 1999).
 - (a) If the cross section and distribution use the same basis functions, it may be possible to find a closed form by following the generator function procedure given by Andrews et al. (1999).
 - (b) If the cross section uses a different basis expansion (for example, Legendre polynomials), it may be possible to use a Gram–Schmidt orthonormalization procedure to express the polynomial factor of one basis in terms of the polynomial (upper-index) factor of the other.

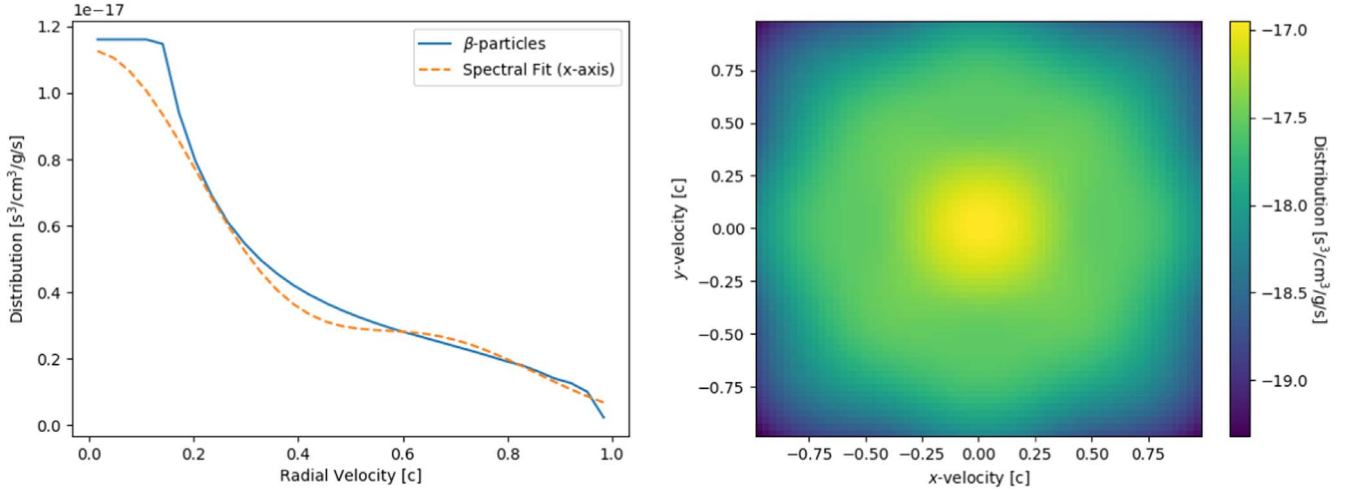


Figure 1. Left: reference uncollided β -particle distribution (blue line) and line out of corresponding spectral reconstruction over $9 \times 9 \times 9$ velocity basis functions (orange-dashed line) vs. radial velocity. The original distribution is calculated from $0.2c$, and is set to a constant for lower velocity. Right: base-10 log of the reconstructed uncollided β -particle distribution vs. the xy -plane of velocity space.

Table 1

Numerical Values of Compact Triple-Hermite Products Using the 1024-point Midpoint Rule Over $\xi \in (-4, 4)$; First Row) and the Closed Form Presented in Appendix B

	$T_c(0, 0, 0)$ $T_c(2, 2, 2)$	$T_c(1, 1, 1)$ $T_c(4, 0, 0)$	$T_c(1, 2, 3)$ $T_c(0, 4, 0)$	$T_c(3, 1, 2)$ $T_c(4, 4, 4)$
Midpoint rule	0.3989422804014322 0.017630924480	0.0 0.0610753139878	0.043186768679 0.0610753139878	0.043186768679 0.001431449
Closed form	0.3989422804014327 0.017630924486	0.0 0.0610753139879	0.043186768684 0.0610753139879	0.043186768684 0.001431452

Note. The function is symmetric under the permutation of the three index arguments, corresponding to each basis order involved in the inner product.

- (c) Determine any index symmetries to further compress the precomputation of the triple product function.
- (d) Identify index selection rules that may increase the sparsity of the triple product function evaluation.

3. Numerical Verification of a Spectral Collision Matrix

In this section, we numerically verify different aspects of the computation of the spectral collision matrix $S_{n,m,p}^{n',n',p'}$, in order to motivate the proof-of-principle 3D KN simulation presented in Section 4. First, we numerically verify the correctness of the compact triple-Hermite products involving one upper-index basis and two lower-index basis functions. Next, we examine spectral expansions of the uncollided β -particle distribution (or the emitted β -particle distribution) and the fast-particle collision kernel. We then verify that the two-parameter coefficient fits used for the closed-form expansion of the cross section match the direct calculation over different values of atomic transition energy. Finally, we compare the numerical integration of Equation (24) directly with the evaluation of Equation (28). For all evaluations of the kernel or cross section, we assume a collision parameter of $\epsilon = 10^{-3}$ in Equation (A11), which corresponds to a minimum collision angle of $\sim 2^\circ.5$. Importantly, in this and the following section, for expanding the β -particle emission and cross sections, we initially transform the kinetic energy into radial velocity using

the relativistic formula,

$$|\mathbf{v}| = c \sqrt{1 - \left(\frac{1}{E_k/(m_e c^2) + 1} \right)^2}, \quad (31)$$

in order to systematically restrict the velocity domain to a more causal region of velocity space. However, the Hermite basis still extends beyond $|\mathbf{v}| = c$.

In Table 1, we compare the closed form of the compact triple-Hermite products (Appendix B, Equation (B21)) to a direct 1024-point midpoint rule numerical integration over the nondimensional velocity domain $\xi \in (-4, 4)$. We see very good agreement for all values, but an increased discrepancy at higher-order basis functions. This seems to be due to the integral bounds in ξ not being extended far enough for accuracy in the direct numerical integration (the bounds are supposed to be indefinite, $\xi \in (-\infty, \infty)$); as the bounds are increased, the implementation of the midpoint rule comes into closer agreement with the closed form across modes.

Turning to the spectral reconstruction of the uncollided β -particle distribution and scatter angle-integrated collision kernel, some numerical experimentation indicates that $\alpha_x = \alpha_y = \alpha_z = 0.5c$ and $u_x = u_y = u_z = 0$ are reasonable basis parameters for both. Figure 1 shows a plot of the uncollided β -particle distribution (solid blue), calculated from the β -particle emission spectrum, and a line out of the spectrally reconstructed profile (orange-dashed line), using Equation (2) with n ,

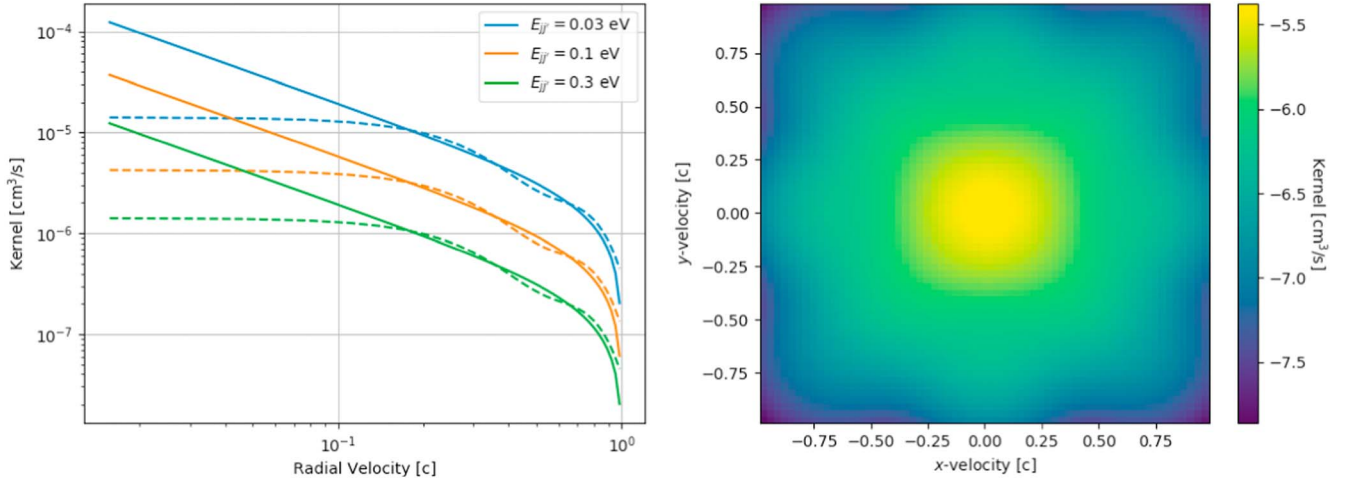


Figure 2. Left: reference one-line scatter angle-integrated kernel (solid line) and line out of corresponding spectral reconstruction kernel over $9 \times 9 \times 9$ velocity basis functions (dashed line), for atomic transition energies of 0.03, 0.1, and 0.3 eV. Right: base-10 log of the reconstructed one-line scatter angle-integrated kernel vs. the xy -plane of velocity space.

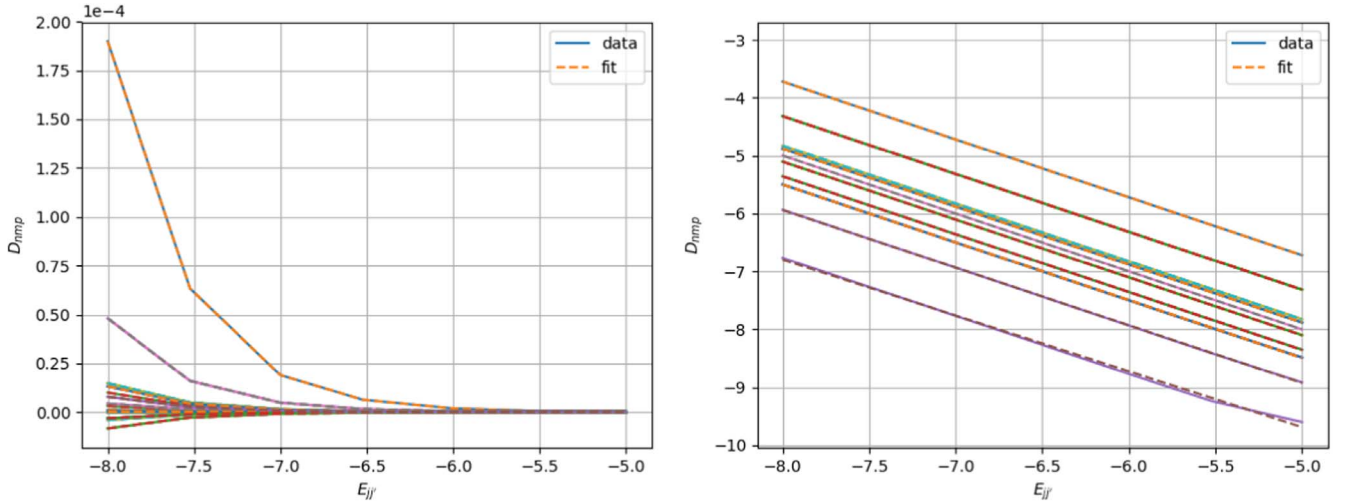


Figure 3. $D_{n,m,p}$ vs. parameterized atomic transition $E_{ij'}$, for a few selected values of (n, m, p) , comparing direct evaluation of the expansion coefficients (solid line) to linear fits in log-log space (dashed line). Left: $D_{n,m,p}$ vs. log base-10 of $E_{ij'}$ in MeV (0.001–10 eV). Right: log base-10 $D_{n,m,p}$ vs. log base-10 of $E_{ij'}$.

m , and p , each ranging from 0–8 in order of Hermite basis. We see some oscillation in the fit, which resembles the well-known Gibbs phenomenon (the ringing artifacts are near high curvature in the profile). The fit is poor for radial velocity below $\sim 0.2c$, where the original distribution is set to a constant. This also is a range where the validity of the fast-particle quantum approximation may start to break down (Inokuti 1971).

The left panel of Figure 2 shows the original (solid line) and reconstructed (dashed line) kernel, where the reconstructed kernel is over the same $9 \times 9 \times 9$ basis as in Figure 1 (again with $\alpha_x = \alpha_y = \alpha_z = 0.5c$ and $u_x = u_y = u_z = 0$). Some oscillation can be seen in the reconstructed kernel as well, and coincidentally, the fit is also poor at radial velocity below $\sim 0.2c$, where error from the original kernel approximation may start to be significant. Furthermore, in the right panel of Figure 2 is a plot of the base-10 log of the reconstructed kernel over the xy -plane in velocity space. While the original kernel is radially symmetric, the reconstructed kernel shows artifacts from fitting over a Cartesian basis of Hermite functions.

Figure 3 shows $D_{n,m,p}$ versus a parameterized transition energy $E_{ij'}$, for a few selected values of (n, m, p) , comparing direct evaluation of the expansion coefficients to linear fits in log-log space. We observe that the linear fits in log-log space do well to capture the dependence of each $D_{n,m,p}$ term for the range of atomic transition energies considered, ~ 0.001 –10 eV. For subsequent calculations involving the construction of the spectral matrix, we use these fits to $D_{n,m,p}$ (which are particularly important for Section 4).

The Hermite basis reconstructions in Figures 1 and 2 suggest orders of 0–8 in each dimension may furnish reasonable accuracy, notwithstanding the approximations already made in the kernel and β -particle emission. We now verify that these Hermite basis orders are sufficient for accuracy when incorporated into the pre-scatter portion of Equation (27). To do so, we compare direct numerical integration of Equation (24) to the evaluation of Equation (28), for a single line with oscillator strength $f_{ij'} = 1$ and transition energy $E_{ij'} = 0.1$ eV. Table 2 has numerical values for some entries of the spectral scattering matrix for direct integration by the midpoint rule on a 64^3 point velocity domain and using

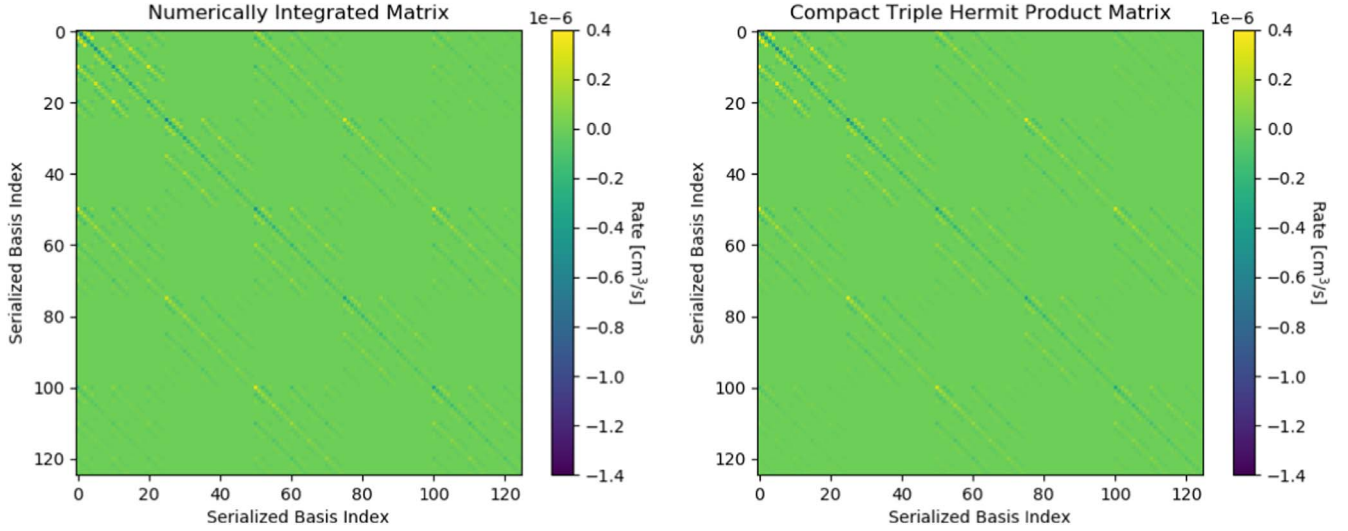


Figure 4. Spectral collision matrix elements vs. matrix indexes serialized over Hermite basis order. Left: a direct numerical integration over the velocity space of Equation (24) using the midpoint rule on a 64^3 velocity grid. Right: evaluation of Equation (28) for each matrix entry.

Table 2
Numerical Values of the Pre-scatter Portion of the Spectral Collision Matrix, and Relative Errors as a Fraction of the Numerical Integral

	$S_{0,0,0}^{0,0,0}$	$S_{0,0,0}^{1,0,0}$	$S_{0,0,0}^{2,0,0}$	$S_{0,0,0}^{3,0,0}$	$S_{0,0,0}^{4,0,0}$
Midpoint rule, Equation (24)	-1.064612e-06 3.773394e-07 -1.838709e-07	-2.244660e-24 1.754513e-24 2.815265e-25	3.773394e-07 -4.477249e-07 3.166727e-07	-3.568146e-24 1.501545e-25 5.027491e-25	-1.838709e-07 3.166727e-07 -3.093139e-07
Equation (28) ($5 \times 5 \times 5$ basis)	-1.035940e-06 3.404054e-07 -1.332969e-07	8.427530e-24 3.839731e-24 -4.118894e-24	3.404054e-07 -3.996374e-07 2.853456e-07	-4.664180e-24 2.175768e-24 1.544883e-24	-1.332969e-07 2.853456e-07 -2.920202e-07
Equation (28) ($9 \times 9 \times 9$ basis)	-1.059921e-06 3.688633e-07 -1.696097e-07	5.339311e-24 7.438594e-24 -5.558943e-24	3.688633e-07 -4.320753e-07 2.999444e-07	-6.485463e-26 1.294707e-24 1.526768e-24	-1.696097e-07 2.999444e-07 -2.977645e-07
Error ($5 \times 5 \times 5$ basis)	0.02693188 0.09788005 0.27505168	4.75447952 1.1884882 15.63057297	0.09788005 0.10740412 0.0989258	0.30717185 13.4901951 2.07287074	0.27505168 0.0989258 0.05590987
Error ($9 \times 9 \times 9$ basis)	0.0044063 0.0224628 0.07756094	3.37867249 3.23969158 20.74571843	0.0224628 0.03495361 0.0528252	0.981824 7.62249883 2.03683885	0.07756094 0.0528252 0.03733877

Note. The top three rows are from direct numerical integration of Equation (24) over a 64^3 point velocity domain using the midpoint rule. The next three rows are from evaluating Equation (28) using compact triple-Hermite products and the fitted data coefficients $D_{n,m,p}$, using $5 \times 5 \times 5$ basis functions. The next three rows are again for Equation (28), but using $9 \times 9 \times 9$ basis functions. The bottom six rows are the relative error between the midpoint rule and Equation (28), as a fraction of the midpoint rule.

Equation (28), with either $5 \times 5 \times 5$ or $9 \times 9 \times 9$ Hermite basis functions. Also in Table 2 is the relative error as a fraction of the direct numerical integral. The matrix elements that are very close numerically to 0 have high errors, but these terms will not contribute to the solution. Otherwise, for the significant entries, we see that the low-order values are in close agreement but along rows/columns of the matrix the error increases with higher disparity between modes, at $\sim 28\%$ for the $S_{0,0,0}^{4,0,0}$ term using $5 \times 5 \times 5$ basis functions. However, in using Equation (28), we do not have to restrict the innermost sum to $5 \times 5 \times 5$, even when simulating $C_{n,m,p}$ modes only up to $5 \times 5 \times 5$. If we permit this innermost sum to go instead to 9 in each velocity dimension, we obtain results with systematically

lower error relative to direct integration ($\lesssim 10\%$ for nontrivial modes). These results indicate that a $9 \times 9 \times 9$ basis truncation of the innermost sum can accurately integrate the matrix terms, consistent with the accuracy of the profile of the truncated kernel expansion shown in Figure 2.

In what follows, we restrict our attention to the pre-scatter matrix since the post-scatter matrix does not complicate the analysis. Again, we assume a single line, a pre-scatter ion population density of 1 (effectively), an atomic transition energy of 0.1 eV, and an oscillator strength of 1. In Figure 4, we show the full matrix for a $5 \times 5 \times 5$ velocity basis function versus serialized matrix indexes. The left panel has the direct numerical integral of Equation (24) for each matrix entry, again

using a midpoint rule over 64^3 points in velocity space, and the right panel uses Equation (28) for each matrix entry (hence using the closed-form compact triple-Hermite product functions). Even over the coarse velocity space grid, the cost of directly numerically integrating the pre-scatter matrix is significantly higher than using the compact triple-Hermite product functions: 1743 s for the numerical integration and 2.2 (5.1) s for the $5 \times 5 \times 5$ ($9 \times 9 \times 9$) innermost sum (using Python/NumPy on a single CPU). This time comparison is, in fact, for a suboptimal implementation of the compact triple-Hermite functions, where they are reevaluated for each instance they are invoked rather than simply precomputed. Moreover, the structure of the matrix matches between the two methods (for this kernel, we observe that much of the qualitative structure comes from the triple products of the Hermite basis function, which can be seen by setting all the $D_{n,m,p}$ values to a constant and comparing to the matrix using detailed atomic data).

4. Trial Calculation of Simplified 3D KN Ejecta Thermalization

In Section 3, we verify the important steps of computing the terms of the spectral matrix $S_{n,m,p}^{n',m',p'}$, which linearly couple together modes of the solution $C_{n,m,p}$. We now apply the $9 \times 9 \times 9$ basis functions used in Section 3, with the parameters $\alpha = 0.5$ and $\mathbf{u} = 0$, to a proof-of-principle KN model in 3D Cartesian spatial geometry. We use the MASS-APP code base, which is a spectral Hermite solver for the Vlasov–Maxwell–Boltzmann equation. The MASS-APP code non-dimensionalizes the equation following Equation (C1); we leverage the reference plasma electron oscillation frequency in Equation (C1) to match the expansion timescale of the KN, setting it to 5×10^{-5} rad s^{-1} . The physical length scale of KNe from 1 day to a week is $\sim 10^{14}$ – 10^{15} cm, which implies the reference plasma oscillation frequency furnishes a nondimensional length scale of $O(1)$. Consequently, we set the 3D spatial domain to a $[-1, 1] \times [-1, 1] \times [-1, 1]$ nondimensional cube.

The KN model has an axisymmetric ejecta with a toroidal (T) component superimposed with a lobed (P; *peanut*) component. The formula for the ion density is derived from the Cassini oval approach of Korobkin et al. (2021),

$$N_a(\bar{x}, \bar{y}, \bar{z}) = N_{a,0} \begin{cases} (1 - \bar{r}^4 + 4\bar{z}^2 - 2\bar{r}^2)^3, & \text{(T),} \\ (1.5 - \bar{r}^4 - 4\bar{z}^2 + 2\bar{r}^2)^3, & \text{(P),} \end{cases} \quad (32)$$

where $N_{a,0}$ is number density, \bar{x} , \bar{y} , and \bar{z} are scaled nondimensional spatial Cartesian coordinates, and $\bar{r}^2 = \bar{x}^2 + \bar{y}^2 + \bar{z}^2$. We set the scaling to 2, so $\bar{\mathbf{r}} = 2\bar{\mathbf{r}}$, where the components of $\bar{\mathbf{r}}$ range from -1 to 1 and are nondimensional in the form of Equation (C1). Considering the typical homologous approximation for KN (or supernova) ejecta, we see that the non-dimensionalization procedure implies,

$$\tilde{\mathbf{x}} = \frac{v_{\text{exp}}}{c} \tilde{t}_{\text{exp}}, \quad (33)$$

where v_{exp} is the bulk expansion velocity of the ejecta, and \tilde{t}_{exp} is the nondimensional time elapsed since the merger event. A nondimensional expansion time of 5 then corresponds to 10^5 s of physical time, or about 1 day, which translates to a physical expansion velocity of $0.2c$ for $\tilde{x} = 1$, $\tilde{z} = \tilde{y} = 0$. This

configuration effectively sets the ejecta velocity scale between the two components to be comparable (Korobkin et al. 2021).

We set the reference number density $N_{a,0}$ for the profile to 10^4 cm^{-3} , which is very low, corresponding to an ejecta mass of $5 \times 10^{-5} M_{\odot}$. This choice approximates the fraction of mass of neodymium (Nd) in a more realistic total (see, for instance, Table 1 of Even et al. 2020); Nd has a significant impact on the photon opacity (Even et al. 2020). The total density profile is a sum over the components where each component imposes a minimum background density of $N_{a,\text{min}} = 10^{-2} \text{ cm}^{-3}$,

$$N_{a,\text{tot}}(\bar{x}, \bar{y}, \bar{z}) = \max(N_{a,\text{min}}, N_{a,0}(1 - \bar{r}^4 + 4\bar{z}^2 - 2\bar{r}^2)^3) + \max(N_{a,\text{min}}, N_{a,0}(1.5 - \bar{r}^4 - 4\bar{z}^2 + 2\bar{r}^2)^3). \quad (34)$$

Figure 5 has isocontour (top panel) and zx -, xy -plane (bottom left and right panels) plots of the ion density given by Equation (32), showing the shape of the combined ejecta components.

The ion temperature is assumed to be isothermal or uniform in space (consistent with thermal electron temperature at late time in some LTE two-temperature KN simulations), and we set it to 0.1 eV. We make an extreme assumption that the entire ejecta is singly ionized Nd, and use energy levels (E_j), statistical weights (g_j), and oscillator strengths $f_{jj'}$ from the LANL suite of atomic physics codes (Fontes et al. 2015b). We neglect oscillator strengths below 10^{-3} , leaving a total of 6888 levels connected by 375,026 lines. Within the singly ionized Nd stage, we determine the excitation levels with the Boltzmann factor and partition function,

$$\int f_{a,j}(\mathbf{v}) d^3v_a = N_{a,j} = \left(\frac{g_j e^{-E_j/T_a}}{\sum_{j'} g_{j'} e^{-E_{j'}/T_a}} \right) N_a, \quad (35)$$

where T_a is the ion temperature. Equation (35) is an assumption of LTE in the excitation states of the ion.

We simulate the model with 10 uniform time steps and 64^3 spatial points over 1 s of physical time, using an initial condition for the β -particle spectrum from Figure 1, proportionally scaling with ejecta density N_a to account for higher β -emission rates at higher ion densities. The initial EM field is set to 0 everywhere ($\mathbf{E} = \mathbf{B} = 0$). On the AMD Rome EPYC 7H12 CPU partition of the HPC system Chicoma at LANL, the simulation took 1.4 hr on 256 cores (we recalculate the matrix entries each time step despite keeping the ion temperature and density as constant in time).

Figure 6 has the kinetic energy gain fraction at 1 s, relative to the initial conditions, in the zx (left) and xy (right) spatial planes. From these plots, we see the kinetic energy loss is enhanced in regions of high density in the ion field as expected, but we also observe a thin layer at the edge of the ejecta where a large fractional gain and loss occur. This effect may be attributable to a transitional region where the ion density is low enough that flux between zones begins to dominate over the collision matrix. We observe in this 1 s timescale that is $\sim 0.3\%$ ($\sim 0.13\%$) of the initial kinetic energy in the β -particle field is lost in density regions near the peak ion density of the torus (peanut) component.

The left panel of Figure 7 has fractional kinetic energy max gain (solid line), max loss (dashed line), and a selected torus/peanut zone versus time for the zx - and xy -planes. We see that

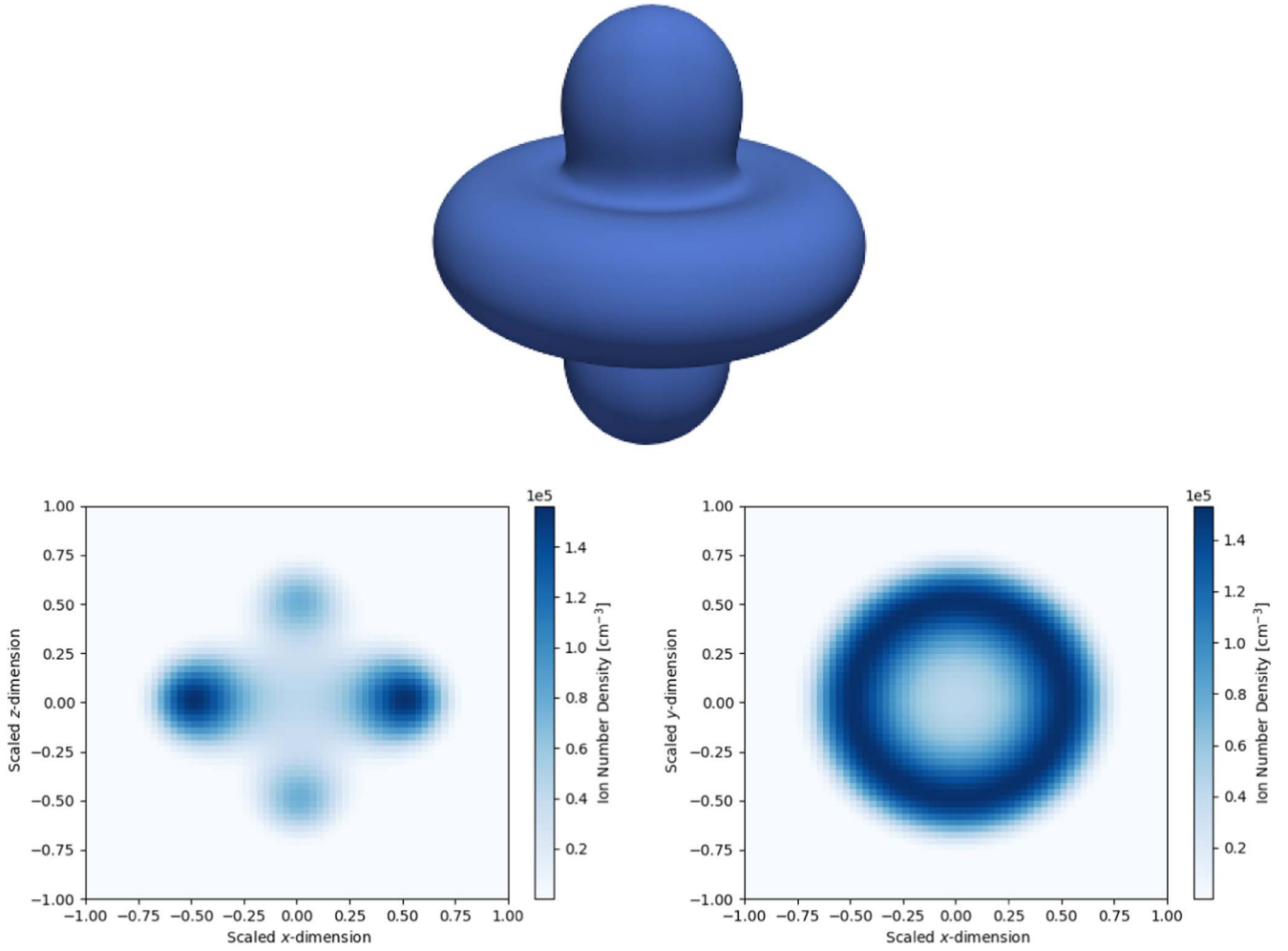


Figure 5. Top: isocontour of 2D axisymmetric KN ejecta morphology from Korobkin et al. (2021; TP morphology) embedded in 3D Cartesian space, showing torus and axial wind components, using Equation (34) with parameters described in Section 4. Bottom: ion number density of the same profile in the zx - (left) and xy - (right) planes.

the fractional kinetic energy losses and gains near the outer edges are higher than losses in the torus and peanut lobes by a factor of a few and an order of magnitude, respectively. It should be noted that these are spatially local fractional values; the energy lost in the torus and peanut lobe is orders of magnitude higher (the fractional metric happens to capture local behavior better, for instance, exposing the effect at the ejecta boundary layer). The right panel of Figure 7 has the corresponding rate of change (time derivative) of the left panel data. The rate of change in the fraction of kinetic energy lost to the ions, relative to the original amount in the spatial zone, is nearly constant over the second for the torus and peanut lobe zones, at approximately $0.3\% \text{ s}^{-1}$ and $0.15\% \text{ s}^{-1}$, respectively, but grows in magnitude for the ejecta boundary layers. Assuming

$$f_{\beta, \text{therm}}(t) \dot{\epsilon}_k(t) \approx \dot{f}_{\beta, \text{therm}}(\epsilon_k(t) - \epsilon_k(0)), \quad (36)$$

where $f_{\beta, \text{therm}}$ is the thermalization fraction and ϵ_k is the kinetic energy emitted by time t , and given that we assumed an emissivity for the initial condition, such that $\epsilon_k(t) - \epsilon_k(0) = \dot{\epsilon}_k(t)$, the rate of change in the fractions result in $f_{\beta, \text{therm}} = 0.003$ (T) or 0.0015 (P).

We may estimate the magnitude of the effect of excitation collision scattering angles $\geq 2^\circ.5$ relative to total β -

thermalization using the semi-analytic formulae of Barnes et al. (2016), in particular their Equation (20) and (32), reproduced here for convenience,

$$\begin{aligned} t_{\beta, \text{ineff}} &= 7.4 \left(\frac{E_k}{0.5 \text{ MeV}} \right)^{-1/2} \left(\frac{M_{\text{ej}}}{5 \times 10^{-3} M_\odot} \right)^{1/2} \left(\frac{v_{\text{exp}}}{0.2c} \right)^{-3/2} \\ &\text{days,} \end{aligned} \quad (37a)$$

$$f_{\beta, \text{therm}}(t) = \frac{\ln(1 + 2(t/t_{\beta, \text{ineff}})^2)}{2(t/t_{\beta, \text{ineff}})^2}, \quad (37b)$$

where $t_{\beta, \text{ineff}}$ is the timescale to inefficient thermalization, which happens to be about where the peak of the KN transient matches the thermalization timescale (Barnes et al. 2016), and $f_{\beta, \text{therm}}$ is again the thermalization fraction at time t , which multiplies the bare emission rate. Using the dimensional values of our 3D model, with $t = 10^5 \text{ s}$ and $v_{\text{exp}} = 0.1c$, and obtaining an average uncollided β -particle energy of 0.3 MeV from integrating $\int E_k f_s(E_k) dE_k / \int f_s(E_k) dE_k$, we see the inefficiency timescale and thermalization fraction for the total β -particle interaction should be roughly 2.7 days and 0.85, respectively.

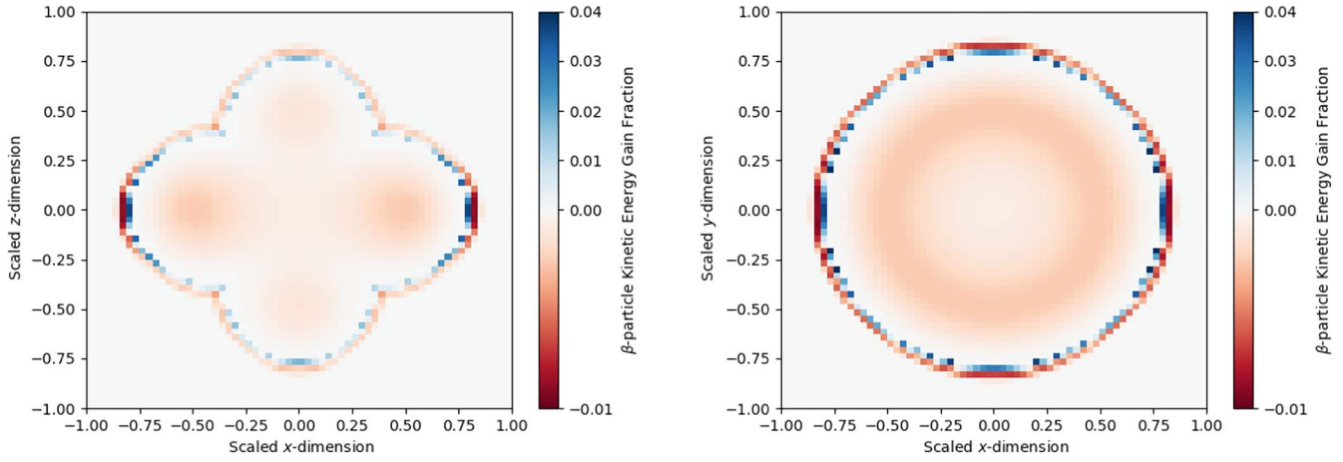


Figure 6. Fraction of kinetic energy gain (blue) and loss (red) from β -particle field in the zx - (left) and xy - (right) planes for the proof-of-principle KN problem described in Section 4.

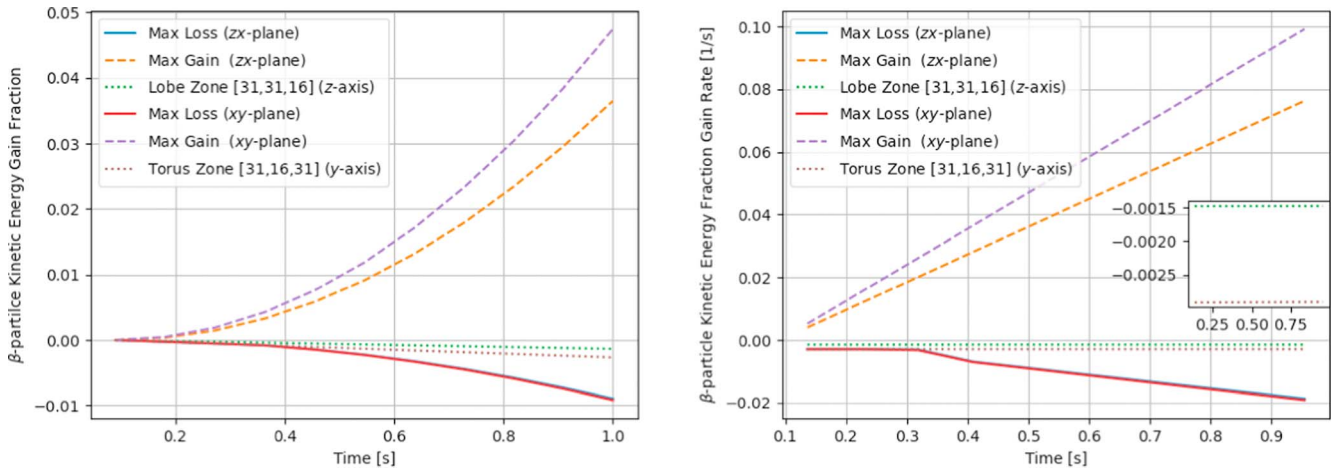


Figure 7. Left: fractional kinetic energy max gain (dashed line), max loss (solid line), and a selected torus/peanut spatial coordinate vs. time for the zx - and xy -planes. Right: corresponding rate of change in fractional kinetic energy, with inset for torus and lobe rates.

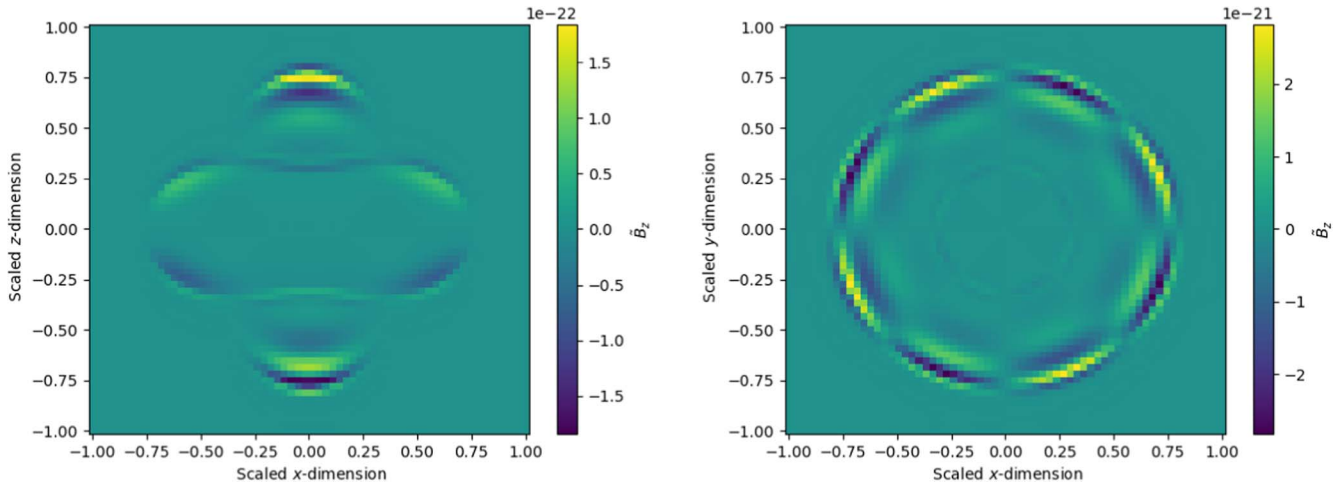


Figure 8. Nondimensional z -component of the magnetic field at 1 s in the zx - (left) and xy - (right) planes, for the proof-of-principle KN problem described in Section 4.

Compared to 0.85, the estimates of 0.003 (T) and 0.0015 (P) are much lower, corresponding to ~ 0.03 day and ~ 0.02 day inefficiency timescales, respectively (using the Newton–Raphson method on Equation (37b)). This indicates excitation

scattering at a large angle is a subdominant but not a vanishingly small mechanism for energy transfer to the ions. Incorporating large-angle ionization and free electron Coulomb collisions may increase the large-angle contribution to

thermalization as well (Barnes et al. 2021). As alluded to earlier, a significant caveat to this numerical evaluation is that the fast-particle approximation has been built into our derivation for large-angle scatters, which for lower-energy β -particles may become invalid.

Given that the Maxwell equation is also being solved, and we started the simulation with $\mathbf{E} = \mathbf{B} = 0$, it may be of interest to see the structure of the magnetic field after 1 s. Figure 8 has the z -component of the nondimensional magnetic field in the zx (left) and xy (right) spatial planes. The nondimensional magnetic field is very low, and nearly 0 everywhere except the edges, again indicating a region where particle flux, and hence current, is important. The nonzero portions show antisymmetry under reflection through the xy -plane, consistent with the 0-divergence condition of the magnetic field. The alternating field in the xy -plane suggests the formation of a very weak long-wavelength EM wave near the surface of the toroidal ejecta. We can see that these values of \tilde{B}_z are subdominant to the collision matrix by examining $C_{0,1,0}$, which corresponds to particle momentum in the y -direction: the time rate of change of $C_{0,1,0}$ is proportional to $\tilde{B}_z C_{1,0,0}$ through the Lorentz force (see Equation (C2)), but it is also proportional to $\sum_{n',m',p'} S_{0,1,0}^{n',m',p'} C_{n',m',p'}$, where the dominant values of $S_{0,1,0}^{n',m',p'}$ are ~ 14 orders of magnitude larger than \tilde{B}_z . As a C-coefficient, the electric field is similarly orders of magnitude lower than the dominant collision matrix elements, but only by ~ 4 orders of magnitude.

5. Conclusions

We have formulated and implemented a preliminary spectral evaluation of the fast-particle atomic excitation kernel presented by Inokuti (1971). The resulting spectral collision matrix couples basis orders in a spatially local way, and balances spatial flux and classical EM terms in the equation governing the time rate of change of the spectral modes. The formulation is restricted to the nonrelativistic, fast-particle kernel, consistent with the Bethe–Born approximation (Bethe 1930), and uses optical oscillator strength data as in photon-matter opacity calculations. This development has been done in the MASS-APP spectral solver framework, which uses Kokkos (Trott et al. 2021) for thread/GPU parallelism and FleCSI (Bergen et al. 2016) to support MPI or Legion-parallel task backends, each layer providing portability and performance on different HPC systems. The code has a full treatment of classical \mathbf{E} and \mathbf{B} fields, thus enabling efficient 3D calculations of KN ejecta β -particle thermalization along with EM effects (which we did not explore with the kernel in this work).

We expand the cross section in terms of the Hermite basis, and find that the simple leading-order dependence of the cross section on atomic bound–bound level transition energy propagates to the expansion coefficients. Moreover, the symmetry of the kernel in radial velocity (in velocity space) implies that these expansion coefficients are symmetric under permutation of the mode/order indexes, and hence, form a compressible low-cost data structure for computer memory when fitted to linear functions in log-coefficient–log-transition energy space. Similarly, the compact triple-Hermite product functions, which build the elements of the spectral scattering matrix, are symmetric under permutation of the mode/order indexes, and obey mode/order parity-based index selection

rules that make them sparse. These compact triple-Hermite product functions also permit interoperability of the spectral collision matrix with adaptive basis coefficients, though we do not test this here.

Numerical results indicate that a reasonable choice of Hermite basis parameters for β -particles in the KN are a bulk velocity parameter $\mathbf{u} = 0$, a thermal velocity parameter of $\alpha = 0.5c$, and a $9 \times 9 \times 9$ mode velocity basis set (Hermite orders 0–8 in each dimension). Section 3 verifies each step in the computation of the spectral collision matrix by comparing compact Hermite triple product functions and matrix elements to the equivalent direct numerical quadrature of the corresponding integrals. Furthermore, in Section 3 we demonstrate the ability to fit the coefficients of the fast-particle cross-section Hermite expansion with linear functions, a property inherited from the leading-order behavior of the differential cross section for small ratios of excitation energy to β -particle kinetic energy. With an implementation of the spectral collision matrix in MASS-APP, we show a proof-of-principle calculation of β -particle propagation and excitation interaction in a 3D snapshot simulation of KN ejecta. Given a lower-bound scattering angle of $\sim 2^\circ.5$ and the caveat of the fast-particle approximation (for instance, using the limit of optical oscillator strengths), this calculation suggests that large-angle scatters of β -particles may not be more than 3 orders of magnitude lower as a power source for the KN luminosity and spectra, not including ionization and free electron Coulomb contributions.

With some further work, the framework should extend to generalized oscillator strengths and the relativistic kernel given by Inokuti (1971), with the caveat that it may be important to replace the Hermite basis with a causally restricted basis (bounding velocity by the speed of light), for instance, using Legendre polynomials as done by Manzini et al. (2017). Another consideration for velocity space is the coordinate system over which the basis functions are expressed. The uncollided β -particle distribution and collision cross section are spherically symmetric in velocity space (though technically, the collision cross section is symmetric about the origin of the center-of-mass frame for each collision), so basis functions in spherical velocity coordinates (for instance, spherical harmonics) may further reduce the size of the basis expansion required for accurate solutions.

Another improvement to fidelity would be to use the homologous expansion velocity of the KN ejecta as the value of the bulk velocity parameter \mathbf{u} in the basis functions, but this may be generally of negligible effect (Barnes et al. 2016). Since \mathbf{u} is variable in spacetime, this would require a modification to the standard spectral system to account for the variation in the equation, but varying the thermal (α) and bulk velocity parameters is an active topic of research (Bessemoulin-Chatard & Filbet 2023; Pagliantini et al. 2023). This would capture some effect of the expansion velocity in the β -particle simulation, permitting a Galilean frame transformation of the kernel.

After adding Coulomb and ionization interactions to the spectral collision matrix, and incorporating both bulk ejecta and microphysical relativistic effects in the kernel, we ultimately intend to use MASS-APP to perform detailed thermalization calculations for β -particles in KN ejecta, subject to different \mathbf{E} and \mathbf{B} field seeds, and use the results to

power photon transfer simulations that synthesize observable light curves and spectra, following Barnes et al. (2021).

Finally, the efficient representation of the coefficients of the Hermite expansion of the cross section as linear in log-log space with respect to atomic transition energy suggests that other cross-section formulae may conform at least approximately to an efficient representation over quantum atomic parameters.

Acknowledgments

This work was supported by the U.S. Department of Energy through the Los Alamos National Laboratory. Los Alamos National Laboratory is operated by Triad National Security, LLC, for the National Nuclear Security Administration of the U.S. Department of Energy (contract No. 89233218CNA000001). The research presented in this article was supported by the Laboratory Directed Research and Development program of Los Alamos National Laboratory under project No. 20220104DR. This research used resources provided by the Los Alamos National Laboratory Institutional Computing Program, which is supported by the U.S. Department of Energy National Nuclear Security Administration under contract No. 89233218CNA000001.

Software: FleCSI (Bergen et al. 2016), Kokkos (Trott et al. 2021), MASS-APP.

Appendix A

Evaluation and Approximation of Kernel Integral

A.1. Evaluation of Maxwellian Integral

For completeness, we give details for evaluating the integral over atom/ion velocity here. We do not assume $\mathbf{v}_{sa} = \mathbf{v}_s$, but instead, show how the same result can be obtained after evaluating the integral over \mathbf{v}_a . Assuming the pre-/post-collision atom/ion distribution is Maxwellian, and that the comoving collision integral is independent of ion/atom velocity, the ion-/atom-dependent velocity integral is

$$\begin{aligned} & \int |\mathbf{v}_a - \mathbf{v}_s| e^{-M_a v_a^2 / 2k_B T} d^3 \mathbf{v}_a \\ &= 2\pi \int_0^\infty \int_{-1}^1 v_{sa}^3 e^{-M_a(v_{sa}^2 + 2v_{sa}v_s\eta + v_s^2) / 2k_B T} d\eta dv_{sa}, \end{aligned} \quad (\text{A1})$$

where η is the cosine of the angle between vectors \mathbf{v}_{sa} and \mathbf{v}_s , and the integral on the right side is over spherical coordinates.

Integrating first over η ,

$$\begin{aligned} & 2\pi \int_0^\infty \int_{-1}^1 v_{sa}^3 e^{-M_a(v_{sa}^2 - 2v_{sa}v_s\eta + v_s^2) / 2k_B T} d\eta dv_{sa} \\ &= 2\pi \int_0^\infty v_{sa}^3 e^{-M_a(v_{sa}^2 + v_s^2) / 2k_B T} \left(\int_{-1}^1 e^{M_a v_{sa} v_s \eta / k_B T} d\eta \right) dv_{sa} \\ &= 2\pi \int_0^\infty v_{sa}^3 e^{-M_a(v_{sa}^2 + v_s^2) / 2k_B T} \left(\frac{2k_B T}{M_a v_{sa} v_s} \sinh \left(\frac{M_a v_{sa} v_s}{k_B T} \right) \right) dv_{sa} \\ &= \frac{4\pi k_B T}{M_a v_s} \int_0^\infty v_{sa}^2 e^{-M_a(v_{sa}^2 + v_s^2) / 2k_B T} \sinh \left(\frac{M_a v_{sa} v_s}{k_B T} \right) dv_{sa}. \end{aligned} \quad (\text{A2})$$

Expressing the hyperbolic sine in terms of exponentials, and completing the squares in the exponents,

$$\begin{aligned} & \frac{4\pi k_B T}{M_a v_s} \int_0^\infty v_{sa}^2 e^{-M_a(v_{sa}^2 + v_s^2) / 2k_B T} \\ & \frac{1}{2} (e^{M_a v_{sa} v_s / k_B T} - e^{-M_a v_{sa} v_s / k_B T}) dv_{sa} \\ &= \frac{2\pi k_B T}{M_a v_s} \int_0^\infty (v_{sa}^2 e^{-M_a(v_{sa} - v_s)^2 / 2k_B T} \\ & - v_{sa}^2 e^{-M_a(v_{sa} + v_s)^2 / 2k_B T}) dv_{sa}, \end{aligned} \quad (\text{A3})$$

where the rightmost integral can be reexpressed as

$$\begin{aligned} & \int_0^\infty (v_{sa}^2 e^{-M_a(v_{sa} - v_s)^2 / 2k_B T} - v_{sa}^2 e^{-M_a(v_{sa} + v_s)^2 / 2k_B T}) dv_{sa} \\ &= \int_{-v_s}^\infty (v + v_s)^2 e^{-M_a v^2 / 2k_B T} dv - \int_{v_s}^\infty (v - v_s)^2 e^{-M_a v^2 / 2k_B T} dv \\ &= \int_{-v_s}^{v_s} v^2 e^{-M_a v^2 / 2k_B T} dv + v_s^2 \int_{-v_s}^{v_s} e^{-M_a v^2 / 2k_B T} dv \\ &+ 2v_s \left(\int_{-v_s}^\infty v e^{-M_a v^2 / 2k_B T} dv + \int_{v_s}^\infty v e^{-M_a v^2 / 2k_B T} dv \right), \end{aligned} \quad (\text{A4})$$

using the substitution $v = v_{sa} - v_s$ ($v = v_{sa} + v_s$) in the integral over the first (second) term. Using

$$\int_{-v_s}^{v_s} e^{-Cv^2} dv = \sqrt{\frac{\pi}{C}} \operatorname{erf}(\sqrt{C} v_s), \quad (\text{A5a})$$

$$\int_{-v_s}^{v_s} v e^{-Cv^2} dv = 0, \quad (\text{A5b})$$

$$2 \int_{v_s}^\infty v e^{-Cv^2} dv = \frac{1}{C} e^{-Cv_s^2}, \quad (\text{A5c})$$

$$\int_{-v_s}^{v_s} v^2 e^{-Cv^2} dv = \frac{1}{2C} \sqrt{\frac{\pi}{C}} \operatorname{erf}(\sqrt{C} v_s) - \frac{v_s}{C} e^{-Cv_s^2}, \quad (\text{A5d})$$

Equation (A4) further reduces to

$$\begin{aligned} & \int_0^\infty (v_{sa}^2 e^{-M_a(v_{sa} - v_s)^2 / 2k_B T} - v_{sa}^2 e^{-M_a(v_{sa} + v_s)^2 / 2k_B T}) dv_{sa} \\ &= \int_{-v_s}^{v_s} v^2 e^{-M_a v^2 / 2k_B T} dv + v_s^2 \int_{-v_s}^{v_s} e^{-M_a v^2 / 2k_B T} dv + 2v_s \left(\int_{-v_s}^\infty v e^{-M_a v^2 / 2k_B T} dv + \int_{v_s}^\infty v e^{-M_a v^2 / 2k_B T} dv \right) \\ &= \frac{k_B T}{M_a} \sqrt{\frac{2\pi k_B T}{M_a}} \operatorname{erf} \left(\sqrt{\frac{M_a}{2k_B T}} v_s \right) - \frac{2k_B T v_s}{M_a} e^{-M_a v_s^2 / 2k_B T} + v_s^2 \sqrt{\frac{2\pi k_B T}{M_a}} \operatorname{erf} \left(\sqrt{\frac{M_a}{2k_B T}} v_s \right) + 2v_s \frac{2k_B T}{M_a} e^{-M_a v_s^2 / 2k_B T} \\ &= \sqrt{\frac{2\pi k_B T}{M_a}} \left(\frac{k_B T}{M_a} + v_s^2 \right) \operatorname{erf} \left(\sqrt{\frac{M_a}{2k_B T}} v_s \right) + \frac{2k_B T v_s}{M_a} e^{-M_a v_s^2 / 2k_B T}. \end{aligned} \quad (\text{A6})$$

Incorporating Equation (A6) into Equation (A1) (via Equation (A2) and (A3)),

$$\begin{aligned}
& \int |v_a - v_s| e^{-M_a v_a^2 / 2k_B T} d^3 v_a \\
&= \frac{2\pi k_B T}{M_a v_s} \left(\sqrt{\frac{2\pi k_B T}{M_a}} \left(\frac{k_B T}{M_a} + v_s^2 \right) \operatorname{erf} \left(\sqrt{\frac{M_a}{2k_B T}} v_s \right) \right. \\
&\quad \left. + \frac{2k_B T v_s}{M_a} e^{-M_a v_s^2 / 2k_B T} \right) \\
&= \left(\frac{2\pi k_B T}{M_a} \right)^{3/2} \frac{1}{v_s} \left(\frac{k_B T}{M_a} + v_s^2 \right) \operatorname{erf} \left(\sqrt{\frac{M_a}{2k_B T}} v_s \right) \\
&\quad + 4\pi \left(\frac{k_B T}{M_a} \right)^2 e^{-M_a v_s^2 / 2k_B T} \\
&= \left(\frac{2\pi k_B T}{M_a} \right)^{3/2} \bar{\Lambda}_a(v_s, T), \tag{A7}
\end{aligned}$$

where we have introduced the function $\bar{\Lambda}_a(v_s, T)$, which represents the atom/ion distribution-weighted average magnitude of difference in velocity between the β -particle and the atom/ions. When $v_s \gg \sqrt{k_B T / M_a}$, Equation (A7) simplifies to

$$\bar{\Lambda}_a(v_s, T) \approx \frac{1}{v_s} \left(\frac{k_B T}{M_a} + v_s^2 \right) \approx v_s. \tag{A8}$$

Thus, we have obtained the inverse of the Maxwellian normalization factor times the magnitude of the β -particle velocity, as desired.

A.2. Solid Angle Integral of the Cross Section

In Section 2, we factor the differential cross section out of the integral over atom/ion velocity, which can be evaluated as

$$\begin{aligned}
& \int \frac{d\sigma_{jj'}}{d\Omega} d\Omega = 4\pi f_{jj'} \left(\frac{e^2}{4E_k} \right)^2 \left(\frac{E_k}{E_{jj'}} \right) \\
&\quad \times \int_{\theta_{\min}}^{\pi} \csc^4(\theta/2) \left[1 - \frac{1}{2} \left(\frac{E_{jj'}}{E_k} \right) \right. \\
&\quad \left. - \left(\sqrt{1 - \left(\frac{E_{jj'}}{E_k} \right)} \right) \cos(\theta) \right] \sin(\theta) d\theta, \tag{A9}
\end{aligned}$$

where θ_{\min} is a minimum scattering angle, which in general may depend on $E_{jj'}$ (but we set it to a constant in this work). Making use of

$$\begin{aligned}
& \int_{\theta_{\min}}^{\pi} \csc^4(\theta/2) \sin(\theta) d\theta \\
&= 4 \int_{-1}^{1-\varepsilon} \frac{d\mu}{(1-\mu)^2} \\
&= 4 \left(\frac{1}{\varepsilon} - \frac{1}{2} \right), \tag{A10a}
\end{aligned}$$

$$\begin{aligned}
& \int_{\theta_{\min}}^{\pi} \csc^4(\theta/2) \cos(\theta) \sin(\theta) d\theta \\
&= 4 \int_{-1}^{1-\varepsilon} \frac{\mu d\mu}{(1-\mu)^2} \\
&= 4 \left(\frac{1-\varepsilon}{\varepsilon} + \frac{1}{2} + \ln(\varepsilon/2) \right), \tag{A10b}
\end{aligned}$$

where $\mu = \cos(\theta)$ and $1 - \varepsilon = \cos(\theta_{\min})$, Equation (A9) becomes

$$\begin{aligned}
& \int \frac{d\sigma_{jj'}}{d\Omega} d\Omega = \sigma_{jj'}(v_s) \\
&= 8\pi f_{jj'} \left(\frac{e^2}{2mv_s^2} \right)^2 \\
&\quad \times \left\{ \left[\left(\frac{mv_s^2}{E_{jj'}} \right) - 1 \right] \left(\frac{1}{\varepsilon} - \frac{1}{2} \right) \right. \\
&\quad \left. - \left[\left(\frac{mv_s^2}{E_{jj'}} \right) \sqrt{1 - \left(\frac{2E_{jj'}}{mv_s^2} \right)} \right] \right. \\
&\quad \left. \times \left(\frac{1-\varepsilon}{\varepsilon} + \frac{1}{2} + \ln(\varepsilon/2) \right) \right\}, \tag{A11}
\end{aligned}$$

where we have used $E_k = m|v_s - \bar{v}_a|^2 / 2 = mv_s^2 / 2$.

Appendix B

Derivation of Compact Hermite Triple Products

B.1. Kernel Expansion and Standard Hermite Triple Products

Expanding the pre-scatter kernel function, written with explicit dependence on a transition energy, in the upper-index basis,

$$\begin{aligned}
& S_c^{(\text{pre})}(v_s, E_{jj'}) \approx \sum_{i_x, i_y, i_z} \\
&\quad \sum_{i_x'', i_y'', i_z''} \\
& \Psi^{i_x'', i_y'', i_z''}(\xi_s) \mathcal{D}_{i_x'', i_y'', i_z''}(E_{jj'}), \tag{B1}
\end{aligned}$$

where $\mathcal{D}_{i_x'', i_y'', i_z''}(E_{jj'})$ depends on transition energy but not on β -particle speed v_s . Incorporating Equation (B1) into the integral for the spectral matrix elements,

$$\begin{aligned}
& S_{i_x', i_y', i_z'}^{i_x, i_y, i_z(\text{pre})} = \int \Psi^{i_x, i_y, i_z}(\xi_s) S_c^{(\text{pre})}(v_s, E_{jj'}) \Psi_{i_x', i_y', i_z'}(\xi_s) d^3 \xi_s \\
&= \sum_{i_x'', i_y'', i_z''} \mathcal{D}_{i_x'', i_y'', i_z''}(E_{jj'}) \\
&\quad \times \int \Psi^{i_x, i_y, i_z}(\xi_s) \Psi_{i_x'', i_y'', i_z''}(\xi_s) \Psi_{i_x', i_y', i_z'}(\xi_s) d^3 \xi_s. \tag{B2}
\end{aligned}$$

Using the standard formulae,

$$\psi^{i_q}(\xi_q) = \frac{1}{\sqrt{2^{i_q} i_q!}} H_{i_q}(\xi_q), \tag{B3a}$$

$$\psi_{i_q}(\xi_q) = \frac{1}{\sqrt{\pi 2^{i_q} i_q!}} H_{i_q}(\xi_q) e^{-\xi_q^2} = \frac{1}{\sqrt{\pi}} \psi^{i_q}(\xi_q) e^{-\xi_q^2}, \tag{B3b}$$

$$\Psi^{i_x, i_y, i_z}(\xi_s) = \psi^{i_x}(\xi_x) \psi^{i_y}(\xi_y) \psi^{i_z}(\xi_z), \tag{B3c}$$

$$\Psi_{i_x, i_y, i_z}(\xi_s) = \psi_{i_x}(\xi_x) \psi_{i_y}(\xi_y) \psi_{i_z}(\xi_z), \tag{B3d}$$

where q denotes x , y , or z , H_{i_q} is the Hermite polynomial of order i_q , and $\xi_s = (\xi_x, \xi_y, \xi_z)$. Incorporating Equation (B3) into the right side of Equation (B2),

$$\begin{aligned}
S_{i_x', i_y', i_z'}^{i_x, i_y, i_z(\text{pre})} &= \sum_{i_x'', i_y'', i_z''}^{I_x, I_y, I_z} \mathcal{D}_{i_x'', i_y'', i_z''}(E_{jj'}) \\
&\int \Psi_{i_x, i_y, i_z}(\xi_s) \Psi_{i_x'', i_y'', i_z''}(\xi_s) \Psi_{i_x', i_y', i_z'}(\xi_s) d^3 \xi_s \\
&= \sum_{i_x'', i_y'', i_z''}^{I_x, I_y, I_z} \mathcal{D}_{i_x'', i_y'', i_z''}(E_{jj'}) \\
&\int \int \int \psi^{i_x}(\xi_x) \psi^{i_y}(\xi_y) \psi^{i_z}(\xi_z) \\
&\psi^{i_x''}(\xi_x) \psi^{i_y''}(\xi_y) \psi^{i_z''}(\xi_z) \psi_{i_x'}(\xi_x) \psi_{i_y'}(\xi_y) \psi_{i_z'}(\xi_z) d\xi_x d\xi_y d\xi_z \\
&= \sum_{i_x'', i_y'', i_z''}^{I_x, I_y, I_z} \mathcal{D}_{i_x'', i_y'', i_z''}(E_{jj'}) \left(\int \psi^{i_x}(\xi_x) \psi^{i_x''}(\xi_x) \psi_{i_x'}(\xi_x) d\xi_x \right) \\
&\left(\int \psi^{i_y}(\xi_y) \psi^{i_y''}(\xi_y) \psi_{i_y'}(\xi_y) d\xi_y \right) \left(\int \psi^{i_z}(\xi_z) \psi^{i_z''}(\xi_z) \psi_{i_z'}(\xi_z) d\xi_z \right)
\end{aligned} \tag{B4}$$

where each 1V integral can be expressed in terms of Hermite polynomials as

$$\begin{aligned}
&\int \psi^{i_q}(\xi_q) \psi^{i_q''}(\xi_q) \psi_{i_q'}(\xi_q) d\xi_q \\
&= \frac{1}{\sqrt{2^{i_q} i_q!} \sqrt{2^{i_q''} i_q''!} \sqrt{\pi 2^{i_q'} i_q'!}} \\
&\times \int H_{i_q}(\xi_q) H_{i_q''}(\xi_q) H_{i_q'}(\xi_q) e^{-\xi_q^2} d\xi_q.
\end{aligned} \tag{B5}$$

The triple-Hermite integral on the right side can be simplified using the result of Andrews et al. (1999; Chapter 6),

$$\begin{aligned}
&\int H_{i_q}(\xi_q) H_{i_q''}(\xi_q) H_{i_q'}(\xi_q) e^{-\xi_q^2} d\xi_q \\
&= \begin{cases} \frac{2^{(i_q+i_q'+i_q'')/2} i_q! i_q'! i_q''! \sqrt{\pi}}{((-i_q+i_q'+i_q'')/2)! ((i_q-i_q'+i_q'')/2)! ((i_q+i_q'-i_q'')/2)!} \\ \text{if } i_q+i_q'+i_q'' \text{ is even and } i_a+i_b \geq i_c \quad \forall (i_a, i_b, i_c) \in \{\text{permutations of } (i_q, i_q', i_q'')\}, \\ 0, \text{ otherwise.} \end{cases}
\end{aligned} \tag{B6}$$

This formula for the triple-Hermite integral is symmetric under permutations of (i_q, i_q', i_q'') , and the requirement of the denominator factorial arguments being positive is equivalent to a discrete triangle inequality for *side lengths* i_q , i_q' , and i_q'' . Moreover, it follows from basic parity arguments that $i_q+i_q'+i_q'' \equiv 0|2 \rightarrow \pm i_q \pm i_q' \pm i_q'' \equiv 0|2$ (replacing pluses with minuses preserves evenness). Incorporating Equation (B6) into Equation (B5), the powers of 2 and π cancel,

$$\begin{aligned}
T(i_q, i_q', i_q'') &\equiv \int \psi^{i_q}(\xi_q) \psi^{i_q'}(\xi_q) \psi_{i_q''}(\xi_q) d\xi_q \\
&= \begin{cases} \frac{\sqrt{i_q! i_q'! i_q''!}}{((-i_q+i_q'+i_q'')/2)! ((i_q-i_q'+i_q'')/2)! ((i_q+i_q'-i_q'')/2)!} \\ \text{if } i_q+i_q'+i_q'' \text{ is even and } i_a+i_b \geq i_c \quad \forall (i_a, i_b, i_c) \in \{\text{permutations of } (i_q, i_q', i_q'')\}, \\ 0, \text{ otherwise,} \end{cases}
\end{aligned} \tag{B7}$$

where $T(i_q, i_q', i_q'')$ is symmetric over all permutations of (i_q, i_q', i_q'') . Using the newly defined $T(i_q, i_q', i_q'')$ in Equation (B4)

$$\begin{aligned}
S_{i_x', i_y', i_z'}^{i_x, i_y, i_z(\text{pre})} &= \sum_{i_x'', i_y'', i_z''}^{I_x, I_y, I_z} \mathcal{D}_{i_x'', i_y'', i_z''}(E_{nn'}) \\
&T(i_x, i_x', i_x'') T(i_y, i_y', i_y'') T(i_z, i_z', i_z'').
\end{aligned} \tag{B8}$$

B.2. Kernel Expansion with Compact Hermite Triple Products

Expanding the pre-scatter kernel function in the lower-index basis,

$$S_c^{(\text{pre})}(v_s, E_{jj'}) \approx \sum_{i_x'', i_y'', i_z''}^{I_x, I_y, I_z} \mathcal{D}_{i_x'', i_y'', i_z''}(E_{jj'}) \Psi_{i_x'', i_y'', i_z''}(\xi_s), \tag{B9}$$

where, as in the preceding section, the $\mathcal{D}_{i_x'', i_y'', i_z''}(E_{jj'})$ coefficients depend on transition energy but not on β -particle speed v_s . The steps for expanding the pre-scatter matrix follow the upper-index formulation, but each 1V integral is now

$$\begin{aligned}
&\int \psi^{i_q}(\xi_q) \psi_{i_q''}(\xi_q) \psi_{i_q'}(\xi_q) d\xi_q = \frac{1}{\sqrt{2^{i_q} i_q!} \sqrt{\pi 2^{i_q''} i_q''!} \sqrt{\pi 2^{i_q'} i_q'!}} \\
&\times \int H_{i_q}(\xi_q) H_{i_q''}(\xi_q) H_{i_q'}(\xi_q) e^{-2\xi_q^2} d\xi_q.
\end{aligned} \tag{B10}$$

The factor of 2 in the exponent of the integral weight implies Equation (B6) cannot be applied directly to Equation (B10). Following Andrews et al. (1999), we may use a three-variable generator function to evaluate the integral on the right side of Equation (B10) as coefficients of the expansion of the generator

function,

$$\begin{aligned}
F(r, s, t) &= \sum_{i_q=0}^{\infty} \sum_{i_q'=0}^{\infty} \sum_{i_q''=0}^{\infty} \frac{1}{i_q! i_q'! i_q''!} \\
&\times \left(\int H_{i_q}(\xi_q) H_{i_q''}(\xi_q) H_{i_q'}(\xi_q) e^{-2\xi_q^2} d\xi_q \right) r^{i_q} s^{i_q'} t^{i_q''},
\end{aligned} \tag{B11}$$

where r , s , and t are the formal variables. Interchanging the sums gives

$$F(r, s, t) = \int \left(\sum_{i_q=0}^{\infty} \frac{1}{i_q!} H_{i_q}(\xi_q) r^{i_q} \sum_{i_q'=0}^{\infty} \frac{1}{i_q'!} H_{i_q'}(\xi_q) s^{i_q'} \sum_{i_q''=0}^{\infty} \frac{1}{i_q''!} H_{i_q''}(\xi_q) t^{i_q''} \right) e^{-2\xi_q^2} d\xi_q. \quad (\text{B12})$$

From Andrews et al. (1999), the sums in parentheses can be evaluated as exponentials,

$$F(r, s, t) = \int (e^{2r\xi_q - r^2} e^{2s\xi_q - s^2} e^{2t\xi_q - t^2}) e^{-2\xi_q^2} d\xi_q. \quad (\text{B13})$$

We complete the square in a different way than Andrews et al. (1999), and evaluate the integral as follows:

$$\begin{aligned} F(r, s, t) &= \int e^{-2\xi_q^2 + 2r\xi_q - r^2 + 2s\xi_q - s^2 + 2t\xi_q - t^2} d\xi_q = \int e^{-(4\xi_q^2 - 4r\xi_q - 4s\xi_q - 4t\xi_q)/2 - r^2 - s^2 - t^2} d\xi_q \\ &= \int e^{-(4\xi_q^2 - 4(r+s+t)\xi_q + (r+s+t)^2)/2 + (r+s+t)^2/2 - (r^2 + s^2 + t^2)} \\ d\xi_q &= e^{(r+s+t)^2/2 - (r^2 + s^2 + t^2)} \int e^{-(2\xi_q - (r+s+t))^2/2} d\xi_q \\ &= e^{rs + st + tr - (r^2 + s^2 + t^2)/2} \int e^{-2(\xi_q - (r+s+t)/2)^2} d\xi_q \\ &= e^{rs + st + tr - (r^2 + s^2 + t^2)/2} \sqrt{\frac{\pi}{2}}. \end{aligned} \quad (\text{B14})$$

In Andrews et al. (1999), only the cross-multiplication terms remained in their equivalent of Equation (B14), which enabled an expansion of the exponential as a product of three series, hence three series indexes that could be related to (i_q, i_q', i_q'') . Here, we introduce six indexes: three for the cross terms and three for the diagonal terms, which makes the system of equation relating (i_q, i_q', i_q'') underdetermined (unlike Andrews et al. 1999). The resulting form of the generator function is

$$\begin{aligned} F(r, s, t) &= \sqrt{\frac{\pi}{2}} e^{rs + st + tr - (r^2 + s^2 + t^2)/2} \\ &= \sqrt{\frac{\pi}{2}} \sum_{a=0}^{\infty} \frac{(rs)^a}{a!} \sum_{b=0}^{\infty} \frac{(st)^b}{b!} \sum_{c=0}^{\infty} \frac{(tr)^c}{c!} \sum_{b'=0}^{\infty} \frac{(-1/2)^{b'} r^{2b'}}{b!} \\ &\quad \sum_{c'=0}^{\infty} \frac{(-1/2)^{c'} s^{2c'}}{c'!} \sum_{a'=0}^{\infty} \frac{(-1/2)^{a'} t^{2a'}}{a'!} \\ &= \sum_{a=0}^{\infty} \sum_{b=0}^{\infty} \sum_{c=0}^{\infty} \\ &\quad \sum_{a'=0}^{\infty} \sum_{b'=0}^{\infty} \sum_{c'=0}^{\infty} \sqrt{\frac{\pi}{2}} \left(-\frac{1}{2} \right)^{a'+b'+c'} \frac{r^{c+a+2b'} s^{a+b+2c'} t^{b+c+2a'}}{a! b! c! a'! b'! c'!}. \end{aligned} \quad (\text{B15})$$

We now introduce the following system of equation in order to re-index the sum:

$$i_q = c + a + 2b', \quad (\text{B16a})$$

$$i_q' = a + b + 2c', \quad (\text{B16b})$$

$$i_q'' = b + c + 2a'. \quad (\text{B16c})$$

Solving Equation (B16) for (a, b, c) in terms of $(i_q, i_q', i_q'', a', b', c')$,

$$a = \frac{i_q + i_q' - i_q''}{2} - (b' + c' - a'), \quad (\text{B17a})$$

$$b = \frac{i_q' + i_q'' - i_q}{2} - (a' + c' - b'), \quad (\text{B17b})$$

$$c = \frac{i_q + i_q'' - i_q'}{2} - (a' + b' - c'). \quad (\text{B17c})$$

From Equation (B17), we obtain the constraint that $i_q + i_q' + i_q''$ must be even, as in the upper-index formulation in Andrews et al. (1999). Furthermore, we notice from Equation (B16) that $2b' \leq i_q$, $2c' \leq i_q'$, and $2a' \leq i_q''$. These index relations imply we can re-

index the sum as follows:

$$F(r, s, t) = \sum_{i_q=0}^{\infty} \sum_{i'_q=0}^{\infty} \sum_{i''_q=0}^{\infty} \delta_{i_q+i'_q+i''_q, 2} \left[\frac{(i_q+i'_q+i''_q)/2}{2} \right] \sqrt{\frac{\pi}{2}} \left(\sum_{a'=0}^{i''_q/2} \sum_{b'=0}^{i_q/2} \sum_{c'=0}^{i'_q/2} \left(-\frac{1}{2} \right)^{a'+b'+c'} \frac{1}{a'!b'!c'!} \right. \\ \left. \frac{\Theta(i_q + i'_q - i''_q - 2(b' + c' - a')) \Theta(i'_q + i''_q - i_q - 2(a' + c' - b')) \Theta(i_q + i''_q - i'_q - 2(a' + b' - c'))}{((i_q + i'_q - i''_q)/2 - (b' + c' - a'))! ((i'_q + i''_q - i_q)/2 - (a' + c' - b'))! ((i_q + i''_q - i'_q)/2 - (a' + b' - c'))!} \right) r^{i_q} s^{i'_q} t^{i''_q}, \quad (\text{B18})$$

where $\delta_{i_q+i'_q+i''_q, 2} \left[\frac{(i_q+i'_q+i''_q)/2}{2} \right]$ is the Kronecker delta function that is 0 (1) when $i_q + i'_q + i''_q$ is odd (even) and $\Theta(\cdot)$ is the discrete step function, which is 0 (1) for negative (positive) argument. We may now unambiguously relate the modified triple integral to analytic closed-form coefficients,

$$\int H_{i_q}(\xi_q) H_{i'_q}(\xi_q) H_{i''_q}(\xi_q) e^{-2\xi_q^2} d\xi_q = \\ i_q! i'_q! i''_q! \delta_{i_q+i'_q+i''_q, 2} \left[\frac{(i_q+i'_q+i''_q)/2}{2} \right] \sqrt{\frac{\pi}{2}} \left(\sum_{a'=0}^{i''_q/2} \sum_{b'=0}^{i_q/2} \sum_{c'=0}^{i'_q/2} \left(-\frac{1}{2} \right)^{a'+b'+c'} \frac{1}{a'!b'!c'!} \right. \\ \left. \frac{\Theta(i_q + i'_q - i''_q - 2(b' + c' - a')) \Theta(i'_q + i''_q - i_q - 2(a' + c' - b')) \Theta(i_q + i''_q - i'_q - 2(a' + b' - c'))}{((i_q + i'_q - i''_q)/2 - (b' + c' - a'))! ((i'_q + i''_q - i_q)/2 - (a' + c' - b'))! ((i_q + i''_q - i'_q)/2 - (a' + b' - c'))!} \right). \quad (\text{B19})$$

The discrete step functions encode the discrete triangle inequality condition discussed in the previous section, but with (i_q, i'_q, i''_q) replaced with $(i_q - 2b', i'_q - 2c', i''_q - 2a')$. Using Equation (B19), Equation (B10) can be written as

$$\int \psi^{i_q}(\xi_q) \psi^{i'_q}(\xi_q) \psi^{i''_q}(\xi_q) d\xi_q = \\ \frac{1}{\sqrt{2\pi} 2^{(i_q+i'_q+i''_q)/2}} \sqrt{i_q! i'_q! i''_q!} \delta_{i_q+i'_q+i''_q, 2} \left[\frac{(i_q+i'_q+i''_q)/2}{2} \right] \left(\sum_{a'=0}^{i''_q/2} \sum_{b'=0}^{i_q/2} \sum_{c'=0}^{i'_q/2} \left(-\frac{1}{2} \right)^{a'+b'+c'} \frac{1}{a'!b'!c'!} \right. \\ \left. \frac{\Theta(i_q + i'_q - i''_q - 2(b' + c' - a')) \Theta(i'_q + i''_q - i_q - 2(a' + c' - b')) \Theta(i_q + i''_q - i'_q - 2(a' + b' - c'))}{((i_q + i'_q - i''_q)/2 - (b' + c' - a'))! ((i'_q + i''_q - i_q)/2 - (a' + c' - b'))! ((i_q + i''_q - i'_q)/2 - (a' + b' - c'))!} \right). \quad (\text{B20})$$

This argument of the sum can be expressed in terms of the $T(\cdot, \cdot, \cdot)$ function defined in Equation (B7) in the preceding section,

$$T_c(i_q, i'_q, i''_q) = \int \psi^{i_q}(\xi_q) \psi^{i'_q}(\xi_q) \psi^{i''_q}(\xi_q) d\xi_q = \\ \frac{1}{\sqrt{2\pi} 2^{(i_q+i'_q+i''_q)/2}} \sqrt{i_q! i'_q! i''_q!} \left(\sum_{a'=0}^{i''_q/2} \sum_{b'=0}^{i_q/2} \sum_{c'=0}^{i'_q/2} \frac{(-1/2)^{a'+b'+c'} T(i_q - 2b', i'_q - 2c', i''_q - 2a')}{a'!b'!c'! \sqrt{(i_q - 2b')! (i'_q - 2c')! (i''_q - 2a')!}} \right), \quad (\text{B21})$$

where the Kronecker delta is included effectively in $T(\cdot, \cdot, \cdot)$ since the condition for $i_q + i'_q + i''_q$ to be even is the same as $i_q - 2b' + i'_q - 2c' + i''_q - 2a'$ (though it might be computationally expedient to check the parity of $i_q + i'_q + i''_q$ prior to any other calculation step). The pre-scatter matrix is obtained by replacing $T(\cdot)$ with $T_c(\cdot)$ in Equation (B8).

Appendix C Full Spectrally Discrete Equation with E and B

The non-dimensionalization of the Maxwell–Boltzmann equation used in MASS-APP is

$$\tilde{t} = \omega_{pe} t, \quad (C1a)$$

$$\tilde{\mathbf{x}} = \frac{\omega_{pe}}{c} \mathbf{x}, \quad (C1b)$$

$$\tilde{\mathbf{v}} = \frac{1}{c} \mathbf{v}, \quad (C1c)$$

$$\tilde{f}_s(\tilde{\mathbf{x}}, \tilde{\mathbf{v}}, \tilde{t}) = \frac{c^3}{N_0} f_s(\mathbf{x}, \mathbf{v}, t), \quad (C1d)$$

$$\tilde{q}_s = \frac{q_s}{e}, \quad (C1e)$$

$$\tilde{m}_s = \frac{m_s}{m_e}, \quad \tilde{M}_a = \frac{M_s}{m_e}, \quad \tilde{M} = \frac{M}{m_e}, \quad (C1f)$$

$$\tilde{\mathbf{E}} = \frac{1}{c} \sqrt{\frac{\varepsilon_0}{m_e N_0}} \mathbf{E}, \quad \tilde{\mathbf{B}} = \sqrt{\frac{\varepsilon_0}{m_e N_0}} \mathbf{B}, \quad (C1g)$$

where ω_{pe} is a reference plasma electron oscillation frequency, c is the speed of light, N_0 is a reference number density, e is electron charge, m_e is electron mass, and ε_0 is permittivity of free space.













The full equation solved in MASS-APP are (dropping the tilde for nondimensionality)

$$\begin{aligned} \frac{\partial C_{n,m,p}}{\partial t} + \nabla \cdot \left(\begin{bmatrix} \alpha_x \sqrt{\frac{n+1}{2}} C_{n+1,m,p} \\ \alpha_y \sqrt{\frac{m+1}{2}} C_{n,m+1,p} \\ \alpha_z \sqrt{\frac{p+1}{2}} C_{n,m,p+1} \end{bmatrix} + C_{n,m,p} \begin{bmatrix} u_x \\ u_y \\ u_z \end{bmatrix} + \begin{bmatrix} \alpha_x \sqrt{\frac{n}{2}} C_{n-1,m,p} \\ \alpha_y \sqrt{\frac{m}{2}} C_{n,m-1,p} \\ \alpha_z \sqrt{\frac{p}{2}} C_{n,m,p-1} \end{bmatrix} \right) - \frac{q_s}{m_s} (\mathbf{E} + \begin{bmatrix} u_x \\ u_y \\ u_z \end{bmatrix} \times \mathbf{B}) \cdot \begin{bmatrix} \frac{\sqrt{2n}}{\alpha_x} C_{n-1,m,p} \\ \frac{\sqrt{2m}}{\alpha_y} C_{n,m-1,p} \\ \frac{\sqrt{2p}}{\alpha_z} C_{n,m,p-1} \end{bmatrix} \\ - \frac{q_s}{m_s} \left(\begin{bmatrix} \alpha_x \\ 0 \\ 0 \end{bmatrix} \times \mathbf{B} \cdot \begin{bmatrix} 0 \\ (\sqrt{nm} C_{n-1,m-1,p} + \sqrt{(n+1)m} C_{n+1,m-1,p})/\alpha_y \\ (\sqrt{np} C_{n-1,m,p-1} + \sqrt{(n+1)p} C_{n+1,m,p-1})/\alpha_z \end{bmatrix} \right) \\ - \frac{q_s}{m_s} \left(\begin{bmatrix} 0 \\ \alpha_y \\ 0 \end{bmatrix} \times \mathbf{B} \cdot \begin{bmatrix} (\sqrt{nm} C_{n-1,m-1,p} + \sqrt{n(m+1)} C_{n-1,m+1,p})/\alpha_x \\ 0 \\ (\sqrt{mp} C_{n,m-1,p-1} + \sqrt{(m+1)p} C_{n,m+1,p-1})/\alpha_z \end{bmatrix} \right) \\ - \frac{q_s}{m_s} \left(\begin{bmatrix} 0 \\ 0 \\ \alpha_z \end{bmatrix} \times \mathbf{B} \cdot \begin{bmatrix} (\sqrt{np} C_{n-1,m,p-1} + \sqrt{n(p+1)} C_{n-1,m,p+1})/\alpha_x \\ (\sqrt{mp} C_{n,m-1,p-1} + \sqrt{m(p+1)} C_{n,m-1,p+1})/\alpha_y \\ 0 \end{bmatrix} \right) = \sum_{n',m',p'} S_{n,m,p}^{n',m',p'} C_{n',m',p'}, \quad (C2a) \end{aligned}$$

$$\frac{\partial \mathbf{B}}{\partial t} = -c \nabla \times \mathbf{E}, \quad (C2b)$$

$$\frac{\partial \mathbf{E}}{\partial t} = c \nabla \times \mathbf{B} - 4\pi q_s \alpha_x \alpha_y \alpha_z \left(C_{0,0,0} \begin{bmatrix} u_x \\ u_y \\ u_z \end{bmatrix} + \frac{1}{\sqrt{2}} \begin{bmatrix} \alpha_x C_{1,0,0} \\ \alpha_y C_{0,1,0} \\ \alpha_z C_{0,0,1} \end{bmatrix} \right). \quad (C2c)$$

ORCID iDs

Ryan T. Wollaeger  <https://orcid.org/0000-0003-3265-4079>
 Chris L. Fryer  <https://orcid.org/0000-0003-2624-0056>
 Robert M. Chiodi  <https://orcid.org/0000-0003-4582-9894>
 Peter T. Brady  <https://orcid.org/0000-0002-4906-2195>
 Oleg Korobkin  <https://orcid.org/0000-0003-4156-5342>
 Cale C. Harnish  <https://orcid.org/0000-0002-2447-3131>
 Christopher J. Fontes  <https://orcid.org/0000-0003-1087-2964>
 Jeffrey R. Haack  <https://orcid.org/0000-0002-2044-0885>
 Oleksandr Chapurin  <https://orcid.org/0000-0002-5321-2838>
 Oleksandr Koshkarov  <https://orcid.org/0000-0002-0935-760X>
 Gian Luca Delzanno  <https://orcid.org/0000-0002-7030-2683>
 Daniel Livescu  <https://orcid.org/0000-0003-2367-1547>

References

- Abbott, B. P., Abbott, R., Abbott, T. D., et al. 2017a, *PhRvL*, **119**, 161101
 Abbott, B. P., Abbott, R., Abbott, T. D., et al. 2017b, *ApJL*, **848**, L12
 Alekseev, I. E., Bakhlanov, S. V., Derbin, A. V., et al. 2020, *PhRvC*, **102**, 064329
 Arcavi, I., Hosseinzadeh, G., Howell, D. A., et al. 2017, *Natur*, **551**, 64
 Armstrong, T. P., Harding, R. C., Knorr, G., & Montgomery, D. 1970, Solution Of Vlasov's Equation By Transform Methods., Technical Report, Univ. of Kansas, Lawrence <https://www.osti.gov/biblio/4079633>
 Andrews, G. E., Askey, R., & Roy, R. 1999, *Special Functions* (Cambridge: Cambridge Univ. Press), 12
 Barnes, J., Kasen, D., Wu, M.-R., & Martínez-Pinedo, G. 2016, *ApJ*, **829**, 110
 Barnes, J., Zhu, Y. L., Lund, K. A., et al. 2021, *ApJ*, **918**, 44
 Bergen, B., Moss, N., & Charest, M. R. J. 2016, Flexible Computer Science Infrastructure FleCSI, Technical Report, Los Alamos National Lab (LANL) <https://www.osti.gov/biblio/1311634>
 Bessemoulin-Chatard, M., & Filbet, F. 2023, *SJNA*, **61**, 1664
 Bethe, H. 1930, *AnP*, **397**, 325
 Bulla, M. 2023, *MNRAS*, **520**, 2558
 Camporeale, E., Delzanno, G. L., Lapenta, G., & Daughton, W. 2006, *PhPI*, **13**, 092110
 Cowperthwaite, P. S., Berger, E., Villar, V. A., et al. 2017, *ApJL*, **848**, L17
 Delzanno, G. L. 2015, *JCoPh*, **301**, 338
 Desai, D., Siegel, D. M., & Metzger, B. D. 2022, *ApJ*, **931**, 104
 Drout, M. R., Piro, A. L., Shappee, B. J., et al. 2017, *Sci*, **358**, 1570
 Even, W., Korobkin, O., Fryer, C. L., et al. 2020, *ApJ*, **899**, 24
 Fermi, E. 1934, *ZPhy*, **88**, 161
 Fontes, C. J., Fryer, C. L., Hungerford, A. L., Wollaeger, R. T., & Korobkin, O. 2020, *MNRAS*, **493**, 4143
 Fontes, C. J., Fryer, C. L., Hungerford, A. L., et al. 2015a, *HEDP*, **16**, 53
 Fontes, C. J., Fryer, C. L., Wollaeger, R. T., Mumpower, M. R., & Sprouse, T. M. 2023, *MNRAS*, **519**, 2862
 Fontes, C. J., Zhang, H. L., Abdallah, J., et al. 2015b, *JPhB*, **48**, 144014
 Freiburghaus, C., Rosswog, S., & Thielemann, F. K. 1999, *ApJL*, **525**, L121
 Fryer, C. L., Hungerford, A. L., Wollaeger, R. T., et al. 2024, *ApJ*, **961**, 9
 Garibotti, C., & Spiga, G. 1994, *JPhA*, **27**, 2709
 Heinzl, J., Coughlin, M. W., Dietrich, T., et al. 2021, *MNRAS*, **502**, 3057
 Hotokezaka, K., Tanaka, M., Kato, D., & Gaigalas, G. 2021, *MNRAS*, **506**, 5863
 Inokuti, M. 1971, *RvMP*, **43**, 297
 Kasen, D., Badnell, N. R., & Barnes, J. 2013, *ApJ*, **774**, 25
 Kasliwal, M. M., Nakar, E., Singer, L. P., et al. 2017, *Sci*, **358**, 1559
 Korobkin, O., Wollaeger, R. T., Fryer, C. L., et al. 2021, *ApJ*, **910**, 116
 Koshkarov, O., Manzini, G., Delzanno, G. L., Pagliantini, C., & Roytershteyn, V. 2021, *CoPhC*, **264**, 107866
 Lattimer, J. M., & Schramm, D. N. 1974, *ApJL*, **192**, L145
 Lattimer, J. M., & Schramm, D. N. 1976, *ApJ*, **210**, 549
 Li, L.-X., & Paczyński, B. 1998, *ApJL*, **507**, L59
 Li, R., Lu, Y., Wang, Y., & Xu, H. 2022, *JCoPh*, **471**, 111650
 Li, R., Lu, Y., & Wang, Y. 2023, *PhFI*, **35**, 102001
 Manzini, G., Funaro, D., & Delzanno, G. L. 2017, *SJNA*, **55**, 2312
 Martin, D., Perego, A., Arcones, A., et al. 2015, *ApJ*, **813**, 2
 Metzger, B. D. 2017, *LRR*, **20**, 3
 Metzger, B. D. 2019, *LRR*, **23**, 1
 Mihalas, D., & Mihalas, B. W. 1984, *Foundations of radiation hydrodynamics* (New York: Oxford Univ. Press)
 Munafò, A., Haack, J. R., Gamba, I. M., & Magin, T. E. 2014, *JCoPh*, **264**, 152
 Pagliantini, C., Delzanno, G. L., & Markidis, S. 2023, *JCoPh*, **488**, 112252
 Perego, A., Rosswog, S., Cabezón, R. M., et al. 2014, *MNRAS*, **443**, 3134
 Pognan, Q., Grumer, J., Jerkstrand, A., & Wanajo, S. 2023, *MNRAS*, **526**, 5220
 Pognan, Q., Jerkstrand, A., & Grumer, J. 2022a, *MNRAS*, **510**, 3806
 Pognan, Q., Jerkstrand, A., & Grumer, J. 2022b, *MNRAS*, **513**, 5174
 Roberts, L. F., Kasen, D., Lee, W. H., & Ramirez-Ruiz, E. 2011, *ApJL*, **736**, L21
 Rosswog, S., Sollerman, J., Feindt, U., et al. 2018, *A&A*, **615**, A132
 Schenter, G., & Vogel, P. 1983, *NSE*, **83**, 393
 Smartt, S. J., Chen, T. W., Jerkstrand, A., et al. 2017, *Natur*, **551**, 75
 Tanaka, M., & Hotokezaka, K. 2013, *ApJ*, **775**, 113
 Tanaka, M., Kato, D., Gaigalas, G., & Kawaguchi, K. 2020, *MNRAS*, **496**, 1369
 Tanvir, N. R., Levan, A. J., González-Fernández, C., et al. 2017, *ApJL*, **848**, L27
 Troja, E., Piro, L., van Eerten, H., et al. 2017, *Natur*, **551**, 71
 Trott, C. R., Lebrun-Grandié, D., Arndt, D., et al. 2021, *IEEE Trans. Parallel Distrib. Syst.*, **33**, 805
 Vencels, J., Delzanno, G. L., Johnson, A., et al. 2015, *Procedia Comput. Sci.*, **51**, 1148
 Villar, V. A., Guillochon, J., Berger, E., et al. 2017, *ApJL*, **851**, L21
 Wang, Y., & Cai, Z. 2019, *JCoPh*, **397**, 108815
 Zhu, Y. L., Lund, K. A., Barnes, J., et al. 2021, *ApJ*, **906**, 94